THE ASTROPHYSICAL JOURNAL SUPPLEMENT SERIES, 97:551–570, 1995 April

NEW MODEL OF IRON SPECTRA IN THE EXTREME ULTRAVIOLET AND APPLICATION TO SERTS AND *EUVE* OBSERVATIONS: A SOLAR ACTIVE REGION AND CAPELLA

N. S. BRICKHOUSE AND J. C. RAYMOND
Harvard-Smithsonian Center for Astrophysics, 60 Garden Street, Cambridge, MA 02138

AND

B. W. SMITH
Los Alamos National Laboratory, SST-9 MS D436, Los Alamos, NM 87545
Received 1994 May 12; accepted 1994 September 22

ABSTRACT

We report new predictions for the EUV spectral emission of Fe IX–Fe XXIV. The iron spectral emission model is the first result of a larger effort to revise the Raymond & Smith model and to update the atomic rates. We present here predicted emissivities for selected densities and temperatures applicable to various astrophysical plasmas. Comparisons of our predicted spectra with two recent observations provide important tests of the atomic data. They also test to some extent some basic assumptions of coronal emission codes: optically thin spectral lines and ionization equilibrium.

Subject headings: atomic processes — stars: coronae — stars: individual (α Aurigae) — Sun: corona — ultraviolet: stars

1. INTRODUCTION

High-quality spectra in the extreme ultraviolet, such as are now available from the Solar EUV Rocket Telescope and Spectrograph (SERTS) (Neupert, Epstein, & Thomas 1992) and the *Extreme Ultraviolet Explorer* (*EUVE*) spectrometers (Welsh et al. 1990), have tremendous diagnostic capability for high temperature plasmas. The ability to resolve a large number of individual emission lines and measure accurate intensities over a wide wavelength range, allows the evaluation of temperatures, densities, and abundances in a variety of astrophysical sources. A number of spectral emission codes exist for various spectral regions, such as Landini & Monsignori Fossi (1990) and Mewe, Gronenschild, & van den Oord (1985). The new observations demand emission codes with high accuracy and a large number of spectral lines (see Mewe 1991). The challenge is to perform critical evaluation of the predictions of these codes relative to observational tests. For any potential diagnostic, assessing the expected accuracy requires checking the valid parameter range, the atomic rate uncertainties, and previous observational tests, as well as the observational errors.

We present here a new model for the EUV emission of highly ionized iron (Fe IX through XXIV). Based on similar physical assumptions as the Raymond & Smith code (Raymond & Smith 1977; Raymond 1988), the new model introduces a number of improvements: the splitting of line multiplets which had previously been lumped together; the solution of the full set of rate equations for each model atom, so that collisions among all levels and cascades can be included; the calculation of the emissivities of numerous weak lines that had previously been omitted; and updated atomic rates.

The aim of our spectral emission code is to predict emission from astrophysical plasmas given a model of the emitting material. The present work assumes an optically thin plasma in ionization equilibrium (based on low-density ionization and recombination rates), with no photoionization. We account for density sensitivity in the collisional excitation rates, solving the full set of statistical equilibrium equations, and including all the available collisional and radiative transition rates among the ion's energy levels. Collision rates are based on Maxwellian velocity distributions. Future work will include nonequilibrium effects such as time dependence, full density sensitivity, radiative transfer in lines, photoionization, and some non-Maxwellian distributions. The EUV results for iron are a natural first step, since transitions among the lower energy levels of iron dominate much of the EUV emission line spectrum. X-ray, UV, and optical lines are included or will be added to our model, as will emission lines from other elements. We present here comparison of our initial results with observational tests, as part of an evaluation of the atomic rates we have adopted.

Predicting individual line intensities rather than the total for multiplets provides more than the convenience of splitting the intensity by wavelength. (We note that the wavelength separations may be large, for example, Fe XXIV λ192.04 and λ255.10 from the $2s2p\,^2P_{3/2}$ and $^2P_{1/2}$, respectively.) For complicated ions, coupling schemes, resonances, relativistic effects, and the number of configurations used in the atomic calculations may affect different fine structure rates differently. Furthermore, electron and proton collisions among states of the ground term at higher densities may have large effects, as can the build-up of considerable population in metastable levels. If some members of a multiplet cannot be observed or are blended, scaling by simple ratios could lead to large errors. The calculation of the weak lines has a dual benefit: where observations exist, agreement of predictions for the weak lines provides additional confidence in the overall assumptions of the model and in the atomic rates; furthermore, the confluence of many weak lines

may appear as a continuum, which can be distinguished from thermal bremsstrahlung.

The current model uses the ionization equilibrium calculated by Arnaud & Raymond (1992). We are able to assess the importance of nonequilibrium effects to some extent through the emission measure modeling described below. In particular, for cases in which discrepancies between observation and prediction might indicate excitation away from the equilibrium temperature, comparison with adjacent ions may suggest instead problems with either the observations or the atomic rates. The chief drawback of the current model is that the effects of high density on dielectronic recombination are not yet included. We provide estimates of this effect using the Raymond & Smith code.

A major improvement over the Raymond & Smith calculation comes from the revision of the collisional excitation rates. We have relied heavily on the evaluated compilation of collisional rates of Pradhan & Gallagher (1992), both for sources of rates and also for assessments of their accuracies. A great deal of interest in improved atomic rates has been generated by the current and upcoming astrophysical missions (*EUVE, ASCA, SOHO, XMM,* and *AXAF*). Moreover, advances in computational atomic physics have led to collision strengths for many rates useful to models of UV- and X-ray–emitting plasmas, notably by participants in the Opacity Project (cf. Seaton 1987) and by the SOHO Atomic Data Project (Lang 1994). For some ions, such as Fe XXI, the collisional rates are now estimated to be accurate to within 10% (Aggarwal 1991). This extremely high accuracy requires the inclusion of relativistic effects and the calculation of resonances near the threshold. Aggarwal finds some effective collision strengths (the collision strength integrated over a Maxwellian temperature distribution) up to an order of magnitude larger than previous results which did not include these threshold effects. For most of the other ions in our model the atomic data are expected to be accurate to 10%–50%, with 30% as a typical figure (cf. Burgess, Mason, & Tully 1993). Given the current interest in these calculations, it is likely that further improvements in the rates for some iron ions will be forthcoming.

The SERTS catalog of an average solar active region (Thomas & Neupert 1994) contains about 270 emission lines from 170 to 450 Å. Of these lines, the authors have identified about 90 lines from Fe IX through Fe XVII which provide coverage of the temperature range from about (4×10^5) to (6×10^6) K. These observations combine excellent spectral and spatial resolution with a relative calibration for the first-order lines (235–450 Å) of ±25%. Each stage of ionization contains at least four lines, so that evaluation of relative line intensities for each model atom is possible.

For more highly ionized iron (Fe XVIII–XXIV), as well as strong lines from Fe IX, XV, and XVI, the EUVE spectrum of Capella (Dupree et al. 1993) demonstrates the rich diagnostic capabilities of the individual line fluxes. Since the initial observation was one of the first spectra obtained by the satellite as part of the calibration program, only the fluxes from the strong lines have been reported to date. Of these strong lines, 22 lines from highly ionized iron are observed, covering the temperature range from about (6×10^5)–(3×10^7) K. The spectral resolution is 0.5 Å in the short-wavelength spectrometer (70–190 Å); 1.0 Å in the medium-wavelength spectrometer (140–380 Å); and 2.0 Å in the long-wavelength band (280–760 Å). With this moderate resolution, significant blending of the lines is possible, and the identifications are supported by constructing an emission model that adequately reproduces the measured fluxes. More than one emission line is observed for several of the iron ions, so that again the redundancy of observations lends confidence in the emission model over some temperature ranges. The flux calibration of the EUVE spectrometers over the entire wavelength range (not including detector edges) is consistent with predicted line ratios of strong unblended lines, for the absorbing interstellar column density derived from UV observations (Linsky et al. 1993). For example, we note that the three strong lines observed in both the medium- and long-wavelength spectrometers agree within ±25%.

The overall agreement between predictions and observations for both sets of data is well within the expected uncertainties. Raymond (1988) has found about ±50% overall agreement for a comparison with lines from a composite solar flare. Lang, Mason, & McWhirter (1990) estimate a standard deviation of about ±60% for quiet Sun EUV lines observed with the CHASE spectrometer. Our overall agreement is better for both the solar active region and Capella. The apparent improvement with our model is undoubtedly a combination of the high-quality data, the avoidance of abundance issues, and the improvements in the atomic rates. We note, however, that for the SERTS spectrum, in particular, the atomic rates for several of the ions are not especially accurate, and, furthermore, density-sensitivity complicates the comparison. These factors are somewhat mitigated by the large number of lines observed for some ions. Thus it is clear that high-quality spectra such as these examples do indeed call for spectral emission codes with improved detail and accuracy.

Comparison with observations requires a knowledge of the distribution of emission measure with temperature. Models for emission measure distributions are derived by minimizing the differences between the observed and predicted intensities. We require integration for each line over the entire temperature range in order to account accurately for the total contribution to the line emission. It is often assumed that the contribution to any individual line comes from a narrow temperature range that is centered on the temperature at which the emitting ion achieves its maximum fraction of the element population. For a flat emission measure distribution, this assumption may be adequate for some ions; however, a steep emission measure distribution, or one with large local minima or maxima, can lead to large contributions to lines from outside the assumed temperature range. Essentially in such a case, the emission from one ionization stage constrains the adjacent ionization stages. We demonstrate the importance of using a full integration.

Unfortunately, neither set of observations here provides a definitive test of the ionization equilibria; however, the expected ratio of Fe XVI to Fe XVII or XVIII varies significantly with different ionization equilibrium models. The extent to which ionization equilibrium is an appropriate model for the physical conditions is a still more difficult question. We will mention the effects of nonequilibrium for resolving the cases

of "outlier" observations where appropriate; however, we are not sufficiently persuaded that the outliers do not result from such mundane effects as atomic rates or measurement uncertainties to drop the working assumption of ionization equilibrium.

A number of density-sensitive lines exist in both observations. Since the emissivities are constrained by other nonsensitive lines and by the emission measure distribution, the uncertainties inherent in line ratio diagnostics for the electron density can be estimated. Thus it is possible to determine whether variations in the densities derived from different line ratios—as much as an order of magnitude (cf. Dere 1982; Mason et al. 1979; Keenan et al. 1994a)—derive from the estimated observational and theoretical uncertainties, or whether such large variations suggest further complexity in the emitting plasma (see Doschek 1984).

2. THE MODEL

2.1. *Ionization Equilibrium*

We adopt the ionization equilibria of Arnaud & Raymond (1992) which use their critically evaluated ionization and recombination rates. The ionization fraction is given for intervals in T_e (K) of 0.1 dex. Compared with the ionization equilibria of Arnaud & Rothenflug (1985), the new model shifts iron to a higher ionization state from log T_e = 5.3–6.0, primarily caused by an increase in the ionization rates. From log T_e = 6.3–7.2, iron is in a lower ionization state, due to an increase in the dielectronic recombination rates. A large discrepancy in the relative ionization fraction of Fe XXIII between solar observations and the Arnaud & Rothenflug model is now resolved by Arnaud & Raymond. The relative concentration of Fe XXIV still appears to be somewhat discrepant with the solar observations. The change that the Arnaud & Raymond ionization balance represents with respect to the Raymond & Smith code is modest.

The ions in our examples which show the largest effects from the newer rates of Arnaud & Raymond are Fe IX, XVI, XVII, and XXIV. For the other ions, the effect of these new rates is typically a shift of 0.1–0.2 dex in temperature. Fe IX is dramatically affected by a shift to lower temperature and by an increase in its peak concentration. Fe XVI is relatively more abundant with respect to Fe XVII. Fe IX and Fe XXIV are at the extremes of the ionization stages observed, and furthermore, Fe XXIV is possibly blended. The effects of the new rates, while substantial for some ions, are difficult to test without an independent measurement of the emission measure distribution and iron abundance.

As we discuss below, the electron densities derived for our two examples are fairly high ($N_e \approx 10^{10}$ cm^{-3} for the SERTS active region and $N_e \approx 10^{11}$–10^{13} cm^{-3} for Capella). The Arnaud & Raymond equilibria are only appropriate for low density plasmas ($\leq 10^{10}$ cm^{-3}). We have explored the effects of density-dependent dielectronic recombination rates (Summers 1974) and metastable populations (Vernazza & Raymond 1979) by using the Raymond & Smith code: an increase by two orders of magnitude in the density affects the population of any given ionization stage by ±15% or less, with the exception of Fe XIV, which decreases by about 30% from $N_e = 10^9$–10^{11} cm^{-3}.

2.2. *Atomic Rates*

This section gives the sources of atomic rates for each ion. Unless otherwise noted, the energies of the levels are the compilations of Corliss & Sugar (1982). We give the sources of electron collisional rates with estimated accuracies, based essentially on assessments of the theoretical techniques used. We fitted the existing data for a Maxwellian temperature distribution over the range from about 10^5 to 10^8 K, using interpolation and extrapolation where necessary, and requiring that the errors from the fits are well below the original uncertainty estimates. Mann (1982) has provided the collisional excitation rates of Mann (1983), with the rates split up among the various fine-structure transitions. These rates are estimated to be accurate to about 30% (Pradhan & Gallagher 1992) and cover a wide energy range beginning at threshold. Proton collisional rates are included in the model assuming $N_H/N_e = 0.8$.

We also list the radiative transition probabilities, which can be important particularly for cases in which metastable levels attain significant populations. (The coronal forbidden lines in the optical arise from these levels, so our model atoms are suitable for these lines at higher densities or at lower densities with a model for photoexcitation.) While we cite the original sources of transition probabilities, we acknowledge here our extensive use of the compilation of Fuhr et al. (1981).

For most ions only $\Delta n = 0$ lines are included. Cascades for higher excitations could increase the intensities of some $\Delta n = 0$ lines, but for the ions we have checked, this cascade contribution is well below 10%.

Fe IX.—The model atom consists of the ground $3p^6\ ^1S_0$ ground state and the 12 levels of the $3p^5 3d$ configuration. Fawcett & Mason (1991) give collision strengths for all 78 possible transitions, at four energies. The contribution of resonances to the collision strengths has not been included in these calculations. We have estimated the resonance contributions using the more approximate of the methods described by Smith et al. (1985) and added these contributions to the rates from the ground state. For a few transitions the resonance contribution is as much as the nonresonant component; for most the effect is less than 30%. It is difficult to assess the accuracy of the resonance estimate, but the contribution is likely to be substantial. The allowed transition probabilities are the optimized values reported by Fawcett & Mason (1991). Forbidden transition probabilities are from Svensson, Ekber, & Edlen (1974), including the magnetic quadrupole λ241.74 observed in the SERTS spectrum, and from Flower (1977).

Fe X.—We include the 31 levels of the $3s^2 3p^5$, $3s 3p^6$, and $3s^2 3p^4 3d$ configurations. Energy levels not given by Corliss & Sugar (1982) are scaled to fit the Corliss & Sugar energies, based on the theoretical energies of Mason (1975). For the lower lying levels excited from the ground multiplet, we use Mason's (1975) collision strengths, assumed independent of energy. Collision strengths among the upper levels are given by Mason & Nussbaumer (1977). Collision strengths are from Mann (1982) for excitations from the ground multiplet to the five highest lying levels. Proton collision rates from the $^2P_{3/2}$ to $^2P_{1/2}$ ground state are from Mason (1975). Oscillator strengths are from Fawcett (1991) and Bromage, Cowan, & Fawcett (1977). We use Mason & Nussbaumer (1977) for the transi-

tion probability of the forbidden line λ257.3, and Edlen & Smitt (1978) for the other forbidden transitions.

Fe XI.—We calculate rates for the $3s^23p^4$, $3s3p^5$, and $3s^23p^33d$ configurations (47 levels), with energies from Corliss & Sugar (1982), Bromage et al. (1977), and Mason (1975). Electron collisions from the $3s^23p^3$ levels, and proton collisions among these levels, are included, again using Mason (1975). Transition rates for allowed transitions are from Mason (1975) and Bromage et al. (1977); forbidden rates are from Mason (1975), and Mason & Nussbaumer (1977), including the upper metastable levels.

Fe XII.—The model atom consists of $3s^23p^3$, $3s3p^4$, and $3s^23p^23d$ configurations (29 levels). Effective collision strengths among the five levels of the $3s^23p^3$ configuration are from Tayal, Henry, & Pradhan (1987), and from these levels to the $3s3p^4$ levels from Tayal & Henry (1988), accurate to within 10% over the temperature range of interest. Collision strengths between $3s^23p^3$ and $3s^23p^23d$ levels are from Flower (1977), accurate to perhaps 30% at the energy chosen (90 eV). Probabilities for allowed transitions are from Tayal & Henry (1986) and Bromage, Cowan, & Fawcett (1978), and from Flower (1977) for the forbidden transitions.

Fe XIII.—We include 23 levels of the $3s^23p^2$, $3s^23p^3$, and $3s^23p3d$ configurations in the model atom. We use the collision strengths from the $3s^23p^2$ levels of Fawcett & Mason (1989) given at three energies, and accurate to within about 30% (Pradhan & Gallagher 1992). Proton collision rates among the ^3P ground levels are from Flower & Pineau des Fôrets (1973). We have taken the allowed transition probabilities from Fawcett (1987) and Flower & Nussbaumer (1974), and the forbidden transition probabilities from Flower & Pineau des Fôrets (1973).

Fe XIV.—We include the 12 levels of $3s^23p$, $3s3p^2$, and $3s^23d$ in our model, with energies given by Redfors & Litzen (1989). Effective collision strengths for all 66 possible transitions are given for log T_e (K) between 5.8 and 7.0 by Dufton & Kingston (1991). The authors discuss the accuracy, presumably better than 30%. Proton collisions from $^2P_{1/2}$ to $^2P_{3/2}$ have been calculated by Heil, Kirby, & Dalgarno (1983). We use Froese-Fischer & Liu (1986) for most transition probabilities, including some forbidden transitions. We use Bhatia & Kastner (1993) for other forbidden transition probabilities. There are fairly large discrepancies (~25%) among various calculated forbidden transition probabilities.

Fe XV.—The model atom has 14 fine-structure levels in the $3s^2$, $3s3p$, $3p^2$, and $3s3d$ configurations. Collision rates from Pradhan (1988) are estimated to be within 20% accuracy (Pradhan & Gallagher 1992). Proton rates from Bhatia & Kastner (1980) for two transitions are used. We have used the allowed transition probabilities of Christensen, Norcross, & Pradhan (1985) and forbidden transition rates for coronal lines from Bhatia & Kastner (1980).

Fe XVI.—The model consists of the five $3s$, $3p$, and $3d$ levels. We use Mann's (1982) collision strengths, which are calculated only from the $3s$ level. We note the recent R-matrix calculations of Tayal (1994), which agree with our effective collision strengths to within 15%. The transition probabilities are from Kim & Cheng (1978).

Fe XVII.—We have used 15 levels in the model atom, the $2p^6\,^1S_0$ ground state, and the $2p^53s$ and $3p$ levels. The energies of Feldman, Doschek, & Seely (1985) are based on solar flare observations. We have used Smith et al.'s (1985) electron excitation rates, including resonances, from the ground level only. These results agree well with the solar X-ray line observations. Chen & Reed (1989) and Goldstein et al. (1989) report more detailed calculations which result in smaller resonance contributions to $2p^53s$ excitation, but these results agree less well with the solar X-ray observations. Bhatia & Doschek (1992) have also computed collision strengths, but they do not include resonances. Unlike other collision rates discussed in this paper, the Smith et al. rates include cascades from upper excited levels. We use Loulergue & Nussbaumer (1975) and Bhatia, Feldman, & Seely (1985) for the transition probabilities.

Fe XVIII.—Our Fe XVIII model consists of the $2s^22p^5\,^2P$ ground levels and the $2s2p^6\,^2S$. The collision strengths from Mohan et al. (1987a, b) and Reed, Chen, & Hazi (1987) are reportedly accurate to 10%. Proton collisions between the ^2P ground levels are from Foster, Keenan, & Reid (1994). Fawcett (1984) gives the transition probabilities.

Fe XIX.—We include nine levels for this ion from the $2s^22p^4$ and $2s2p^5$ configurations. We use Mann's (1982) collision strengths from the ^3P ground levels. Electron and proton collisions among the ^3P levels are calculated by Loulergue et al. (1985). Allowed transition probabilities are those of Cheng, Kim, & Desclaux (1979) and forbidden transitions are those of Loulergue et al. (1985).

Fe XX.—The Fe XX model atom consists of the 13 levels of the $2s^22p^3$ and $2s2p^4$ configurations. Collision strengths calculated by Mann (1982) are from the $^4S_{3/2}$ ground level up to the $2s^22p^3$ configuration only. We use for the other transitions the collision strengths of Bhatia & Mason (1980), given at three energies, as well as their proton collision rates. Allowed transitions are from Cheng et al. (1979), and intersystem transition probabilities are from Bhatia & Mason (1980).

Fe XXI.—The model atom consists of the $2s^22p^2$ and $2s2p^3$ configurations (15 levels). Effective collision strengths from Aggarwal (1991) are for all possible transitions and are considered to be 10% accurate. Proton collisions rates are from Faucher (1977). Allowed transitions are from Cheng et al. (1979); forbidden transitions are from Mason et al. (1979).

Fe XXII.—We use a 10 level model atom for Fe XXII with the $2s^22p$ ground state levels and the $2s2p^2$ levels. Collision strengths are from Mann (1982), which compare well with Mason & Storey (1980) except for an apparent switch in Mann's labels for two transitions. They agree with recent relativistic distorted wave calculations by Zhang & Sampson (1995) to within ~10% for the permitted lines and ~25% for intercombination lines. We expect that resonance contributions to some collision strengths are significant, but we have not included estimates. Cascades from $2s^23p$ contribute less than 10%. Proton rates are from Mason & Storey (1980). Allowed transition probabilities are from Cheng et al. (1979); forbidden transition rates are from Bhatia, Feldman, & Seely (1986).

Fe XXIII.—The model atom consists of the eight levels of the $2s^2$, $2s2p$, and $2p^2$ configurations. The effective collision strengths of Keenan et al. (1993) should be accurate to 10%.

The proton rates are Doyle's (1987). Allowed transitions are given by Cheng et al. (1979); the forbidden transition probability for $^3P_1$–$^3P_0$ is given by Idrees & Das (1989).

Fe XXIV.—This model atom is a three-level system ($2s$ and $2p$ states). Hayes (1979) gives collision strengths accurate to about 20% (Pradhan & Gallagher 1992). Cheng et al. (1979) give the transition probabilities. Cascades from the $3s$ and $3d$ levels contribute only a few percent to these lines.

2.3. *Emissivities*

Table 1 gives the results of the solution of the statistical equilibrium equations. This model assumes an abundance for iron of 7.6 (Allen 1973). The table gives line emissivities for the given temperatures calculated for an electron density $N_e = 10^{10}$ cm^{-3}. The radiation P_λ for a given line is tabulated for $P_\lambda \geq 10^{-29}$ ergs cm^3 s^{-1}. Multiplying P_λ by the emission measure, $\int N_e N_H dV$, gives the total power radiated at the source. Not all transitions in the model are presented in Table 1; only the strongest lines, and other lines chosen for illustrative purposes are included. It is important to keep in mind that several of the lines in Table 1 are blended with strong lines of other elements.

Table 2 shows how the density-sensitive lines (those lines which show more than a factor of ~20% change with density) vary from $N_e = 10^8$ to 10^{13} cm^{-3}. To generate this table, we used the line emissivity at the temperature of maximum ionization fraction for the densities listed. Relative variations with temperature between two lines of the same ion should be small in most cases. The two tables presented here are intended to provide a useful list of strong lines, and a rough estimate of their expected relative intensities.[1]

3. COMPARISON WITH OBSERVATIONS

This section presents an assessment of the model in view of the two sets of observations, comparing predictions with observations by three methods. First we consider the branching ratios for transition lines formed at the same upper level. The modeling assumption is simple: we need only consider relative radiative transition rates for an optically thin plasma.

Second, we consider the relative line intensities for each ion. We perform the full statistical solution for all of the model ions here; for most of these iron systems, complexity requires this solution at higher densities. For a few ions, the coronal approximation would be adequate, so that the line ratios of strong resonance lines are proportional to the collisional excitation rates from the ground state. These few cases and the branching ratios provide a good figure of merit for the quality of the flux measurements as well as a check on the assumption that $\tau \approx 0$. For all of the lines from both data sets we have calculated line intensities over a range of at least two orders of magnitude in density in order to assess the effects of density sensitivity. We emphasize that the effects of density can be large even for strong resonance transitions because the ground state becomes depleted. The strong Fe IX λ171.07 line decreases by a factor of 2 over the density range from 10^9 to 10^{11} cm^{-3}, due to transfer of population to a low-lying metastable level. Similarly, the Fe XXI resonance transition λ128.73 decreases by nearly a factor of 2 between 10^{11} and 10^{13} cm^{-3} as the ground state is depopulated.

As a third observational test of the model, we have constructed emission measure distributions for the two data sets over the entire temperature range for which the iron spectra are observed. Adjacent ionization stages constrain the emission measure at any given temperature, giving further confidence in the rates used (as well as helping to establish plausible sources of problems).

3.1. *Branching Ratios*

The branching ratio is simply the ratio of radiative transition rates of two lines which share a common upper fine-structure level; the uncertainty of the theoretical branching ratio is therefore, that of the two transition rates (which for most of the iron lines with branching ratios should be ~25% each). As long as lines are intense and unblended, the major source of observational error is the relative calibration over wavelength.

Table 3 lists the observed lines from the two data sets for which branching ratios may be compared, the theoretical ratios used in our model, and a number of comparison observations. We note that other theoretical calculations for these branching ratios are consistent to within ±30%, except for a few cases, as noted in the table.

Other observations listed include two full disk solar spectra, both of which overlap substantial portions of the SERTS spectrum. Whereas Behring et al. (1976) claim relative intensity calibration of ±30% only for lines close in wavelength, the Malinovsky & Heroux (1973) spectrum was photometrically calibrated to ±25% over the entire wavelength range.

We also include the PLT Tokamak data (Stratton, Moos, & Finkenthal 1984 and Stratton et al. 1985) which overlap with the *EUVE* spectral region. The tokamak spectrum has a spectral resolution of approximately ±0.7 Å and wavelength identification to within ±0.2 Å. The accuracy of the relative intensities is conservatively estimated to be ±30%. The tokamak data are particularly useful for substantiating the presence or absence of blends—since the tokamak plasma temperature and density are measured independently and locally, the observational test of the line intensities is better constrained than for an astrophysical plasma.

Table 3 shows that most branching ratios agree to within their expected limits (factors of 2); however, a number of problem cases arise. For the Fe XI transitions from the $3s3p^5\ ^3P_1$ level, one might suspect that the transition to the $3s^23p^4\ ^3P_0$ (λ358.64) is problematic since the other branching ratio from this upper level is acceptable. Indeed, in the SERTS spectrum, the λ358.64 line is roughly 50% wider than other lines nearby in wavelength, leading us to suspect that it is blended. A major discrepancy between the prediction and the observation occurs for the Fe XIII λ201.12/λ204.94 ratio. Both full disk observations are consistent with the model, and there is no reason to suspect the relative calibration of two lines so close together. The contribution from Fe XII λ201.12 would be significant

[1] The full results of the emissivity calculation for N_e from 10^8 to 10^{13} cm^{-3}, and log T_e(K) from 5.4 to 7.8 (in 0.1 dex intervals) are available electronically from bhouse@cfa.harvard.edu.

TABLE 1

LINE EMISSION ($-\log [P_\lambda(\text{ergs cm}^3\ \text{s}^{-1})] - 23.0$)

λ (Å)	Upper Level	Lower Level	$log[T_e(K)]$										
FeIX			**5.4**	**5.5**	**5.6**	**5.7**	**5.8**	**5.9**	**6.0**	**6.1**	**6.2**	**6.3**	**6.4**
171.07	$3s^23p^53d\ ^1P_1$	$3s^23p^6\ ^1S_0$	1.74	0.69	0.07	-0.26	-0.40	-0.38	-0.13	0.52	1.58	3.09	5.02
217.10	$3s^23p^53d\ ^3D_1$	$3s^23p^6\ ^1S_0$	3.08	2.13	1.60	1.34	1.29	1.37	1.69	2.41	3.53	5.10	···
241.74	$3s^23p^53d\ ^3P_2$	$3s^23p^6\ ^1S_0$	2.93	1.98	1.44	1.18	1.11	1.18	1.48	2.18	3.30	4.85	···
244.91	$3s^23p^53d\ ^3P_1$	$3s^23p^6\ ^1S_0$	3.11	2.16	1.63	1.38	1.33	1.42	1.75	2.47	3.61	5.19	···
FeX			**5.5**	**5.6**	**5.7**	**5.8**	**5.9**	**6.0**	**6.1**	**6.2**	**6.3**	**6.4**	**6.5**
170.58	$3s^23p^4(^3P)3d\ ^2D_{3/2}$	$3s^23p^5\ ^2P_{3/2}$	···	4.38	3.28	2.50	1.98	1.79	2.06	2.80	4.01	5.69	···
174.53	$3s^23p^4(^3P)3d\ ^2D_{5/2}$	$3s^23p^5\ ^2P_{3/2}$	3.99	2.46	1.39	0.63	0.14	-.03	0.27	1.03	2.25	3.94	···
175.27	$3s^23p^4(^3P)3d\ ^2D_{3/2}$	$3s^23p^5\ ^2P_{1/2}$	4.64	3.08	1.99	1.20	0.69	0.49	0.77	1.51	2.72	4.40	···
175.47	$3s^23p^4(^3P)3d\ ^2P_{1/2}$	$3s^23p^5\ ^2P_{3/2}$	5.52	3.97	2.89	2.11	1.61	1.42	1.70	2.44	3.66	5.34	···
177.24	$3s^23p^4(^3P)3d\ ^2P_{3/2}$	$3s^23p^5\ ^2P_{3/2}$	4.28	2.75	1.69	0.93	0.44	0.27	0.56	1.32	2.54	4.23	···
180.41	$3s^23p^4(^3P)3d\ ^2P_{1/2}$	$3s^23p^5\ ^2P_{1/2}$	5.03	3.48	2.40	1.62	1.11	0.92	1.21	1.95	3.17	4.85	···
182.31	$3s^23p^4(^3P)3d\ ^2P_{3/2}$	$3s^23p^5\ ^2P_{1/2}$	5.83	4.30	3.24	2.48	1.98	1.81	2.11	2.87	4.09	5.78	···
184.54	$3s^23p^4(^1D)3d\ ^2S_{1/2}$	$3s^23p^5\ ^2P_{3/2}$	4.54	3.02	1.96	1.21	0.72	0.55	0.85	1.60	2.83	4.52	···
190.04	$3s^23p^4(^1D)3d\ ^2S_{1/2}$	$3s^23p^5\ ^2P_{1/2}$	5.09	3.57	2.51	1.76	1.27	1.10	1.40	2.16	3.38	5.07	···
225.29	$3s^23p^4(^3P)3d\ ^4P_{5/2}$	$3s^23p^5\ ^2P_{3/2}$	5.74	4.27	3.25	2.54	2.08	1.95	2.27	3.06	4.31	6.03	···
257.26	$3s^23p^4(^3P)3d\ ^4D_{5/2}$	$3s^23p^5\ ^2P_{3/2}$	5.70	4.24	3.23	2.52	2.07	1.94	2.26	3.05	4.30	6.02	···
257.30	$3s^23p^4(^3P)3d\ ^4D_{7/2}$	$3s^23p^5\ ^2P_{3/2}$	5.63	4.14	3.10	2.36	1.88	1.71	2.01	2.77	4.00	5.69	···
345.75	$3s3p^6\ ^2S_{1/2}$	$3s^23p^5\ ^2P_{3/2}$	5.04	3.62	2.65	1.97	1.54	1.41	1.75	2.55	3.80	5.53	···
365.57	$3s3p^6\ ^2S_{1/2}$	$3s^23p^5\ ^2P_{1/2}$	5.42	4.00	3.03	2.35	1.91	1.79	2.13	2.92	4.18	5.90	···
FeXI			**5.5**	**5.6**	**5.7**	**5.8**	**5.9**	**6.0**	**6.1**	**6.2**	**6.3**	**6.4**	**6.5**
178.10	$3s^23p^3(^4S)3d\ ^3D_2$	$3s^23p^4\ ^3P_2$	···	···	4.59	3.19	2.17	1.56	1.47	1.89	2.84	4.28	5.82
179.76	$3s^23p^3(^2D)3d\ ^1F_3$	$3s^23p^4\ ^1D_2$	···	···	4.16	2.72	1.67	1.05	0.94	1.37	2.32	3.76	5.30
180.40	$3s^23p^3(^4S)3d\ ^3D_3$	$3s^23p^4\ ^3P_2$	···	5.26	3.43	2.04	1.03	0.44	0.35	0.79	1.75	3.19	4.73
180.60	$3s^23p^3(^4S)3d\ ^3D_1$	$3s^23p^4\ ^3P_1$	···	···	4.45	3.05	2.02	1.41	1.31	1.74	2.68	4.12	5.66
181.10	$3s^23p^3(^4S)3d\ ^3D_1$	$3s^23p^4\ ^3P_0$	···	···	4.30	2.91	1.88	1.27	1.17	1.60	2.54	3.98	5.52
182.20	$3s^23p^3(^4S)3d\ ^3D_2$	$3s^23p^4\ ^3P_1$	···	5.80	3.94	2.53	1.51	0.90	0.81	1.23	2.18	3.62	5.16
184.70	$3s^23p^3(^2D)3d\ ^3P_1$	$3s^23p^4\ ^3P_2$	···	···	4.32	2.93	1.92	1.31	1.23	1.66	2.61	4.06	5.59
184.80	$3s^23p^3(^2D)3d\ ^1D_2$	$3s^23p^4\ ^1D_2$	···	···	4.43	3.00	1.96	1.33	1.23	1.66	2.61	4.05	5.59
188.22	$3s^23p^3(^2D)3d\ ^3P_2$	$3s^23p^4\ ^3P_2$	···	5.45	3.62	2.24	1.24	0.64	0.56	1.00	1.96	3.40	4.94
189.02	$3s^23p^3(^2D)3d\ ^3P_0$	$3s^23p^4\ ^3P_1$	···	···	4.49	3.09	2.06	1.45	1.36	1.78	2.73	4.17	5.71
189.10	$3s^23p^3(^2D)3d\ ^3P_1$	$3s^23p^4\ ^3P_1$	···	···	4.45	3.06	2.05	1.45	1.36	1.79	2.75	4.19	5.73
189.70	$3s^23p^3(^2D)3d\ ^3P_1$	$3s^23p^4\ ^3P_0$	···	···	4.52	3.13	2.11	1.51	1.42	1.86	2.81	4.25	5.79
192.02	$3s^23p^3(^2D)3d\ ^3S_1$	$3s^23p^4\ ^3P_1$	···	···	4.64	3.26	2.26	1.66	1.58	2.01	2.97	4.41	5.96
192.82	$3s^23p^3(^2D)3d\ ^3P_2$	$3s^23p^4\ ^3P_1$	···	···	4.33	2.95	1.95	1.35	1.27	1.71	2.67	4.11	5.65
201.74	$3s^23p^3(^2D)3d\ ^3S_1$	$3s^23p^4\ ^1D_2$	···	···	4.33	2.95	1.94	1.34	1.26	1.70	2.65	4.10	5.64
204.60	$3s^23p^3(^2D)3d\ ^1P_1$	$3s^23p^4\ ^1D_2$	···	···	4.42	3.01	1.98	1.37	1.28	1.71	2.66	4.11	5.65
348.97	$3s3p^5\ ^3P_0$	$3s^23p^4\ ^3P_1$	···	···	5.10	3.76	2.79	2.22	2.15	2.60	3.57	5.03	···
358.64	$3s3p^5\ ^3P_1$	$3s^23p^4\ ^3P_0$	···	···	4.97	3.65	2.69	2.12	2.07	2.53	3.50	4.96	···
352.68	$3s3p^5\ ^3P_2$	$3s^23p^4\ ^3P_2$	···	5.99	4.23	2.91	1.96	1.40	1.35	1.81	2.79	4.25	5.80
406.84	$3s3p^5\ ^3P_2$	$3s^23p^4\ ^1D_2$	···	···	6.12	4.80	3.84	3.29	3.23	3.70	4.67	6.13	···
FeXII			**5.7**	**5.8**	**5.9**	**6.0**	**6.1**	**6.2**	**6.3**	**6.4**	**6.5**	**6.6**	**6.7**
186.86	$3s^23p^2(^3P)3d\ ^2F_{5/2}$	$3s^23p^3\ ^2D_{3/2}$	···	4.63	3.06	2.00	1.52	1.63	2.30	3.51	4.84	···	···
186.88	$3s^23p^2(^3P)3d\ ^2F_{7/2}$	$3s^23p^3\ ^2D_{5/2}$	···	3.98	2.40	1.33	0.85	0.95	1.62	2.82	4.13	5.42	···
188.17	$3s^23p^2(^3P)3d\ ^2D_{3/2}$	$3s^23p^3\ ^2P_{1/2}$	···	4.85	3.28	2.22	1.74	1.85	2.52	3.74	5.07	···	···
190.06	$3s^23p^2(^1S)3d\ ^2D_{3/2}$	$3s^23p^3\ ^4S_{3/2}$	···	4.91	3.32	2.23	1.73	1.80	2.45	3.62	4.91	···	···
191.04	$3s^23p^2(^3P)3d\ ^2D_{5/2}$	$3s^23p^3\ ^2P_{3/2}$	···	4.19	2.61	1.54	1.06	1.15	1.81	3.01	4.32	5.61	···
192.39	$3s^23p^2(^3P)3d\ ^4P_{1/2}$	$3s^23p^3\ ^4S_{3/2}$	···	4.08	2.49	1.39	0.89	0.96	1.60	2.76	4.05	5.31	···
193.51	$3s^23p^2(^3P)3d\ ^4P_{3/2}$	$3s^23p^3\ ^4S_{3/2}$	5.73	3.66	2.07	0.97	0.47	0.53	1.17	2.34	3.62	4.88	···
195.12	$3s^23p^2(^3P)3d\ ^4P_{5/2}$	$3s^23p^3\ ^4S_{3/2}$	5.51	3.44	1.85	0.75	0.25	0.31	0.95	2.12	3.40	4.66	···
195.19	$3s^23p^2(^1D)3d\ ^2D_{3/2}$	$3s^23p^3\ ^2D_{3/2}$	···	4.49	2.92	1.86	1.38	1.48	2.15	3.35	4.67	5.96	···
196.64	$3s^23p^2(^1D)3d\ ^2D_{5/2}$	$3s^23p^3\ ^2D_{5/2}$	···	4.31	2.75	1.68	1.20	1.30	1.97	3.18	4.49	5.79	···
200.36	$3s^23p^2(^1D)3d\ ^2S_{1/2}$	$3s^23p^3\ ^2P_{3/2}$	···	5.08	3.51	2.45	1.98	2.08	2.76	3.97	5.30	···	···
201.12	$3s^23p^2(^1D)3d\ ^2P_{3/2}$	$3s^23p^3\ ^2P_{3/2}$	···	4.89	3.32	2.25	1.78	1.88	2.56	3.77	5.10	···	···
203.27	$3s^23p^2(^1S)3d\ ^2D_{5/2}$	$3s^23p^3\ ^2D_{5/2}$	···	4.67	3.10	2.03	1.54	1.63	2.29	3.48	4.78	···	···
206.37	$3s^23p^2(^1S)3d\ ^2D_{3/2}$	$3s^23p^3\ ^2D_{3/2}$	···	4.78	3.19	2.11	1.61	1.68	2.32	3.49	4.78	···	···
211.74	$3s^23p^2(^3P)3d\ ^2P_{1/2}$	$3s^23p^3\ ^2D_{3/2}$	···	4.51	2.92	1.84	1.34	1.41	2.06	3.23	4.52	5.79	···
217.27	$3s^23p^2(^3P)3d\ ^2P_{3/2}$	$3s^23p^3\ ^2D_{3/2}$	···	4.87	3.30	2.25	1.77	1.87	2.54	3.74	5.06	···	···
219.44	$3s^23p^2(^3P)3d\ ^2P_{3/2}$	$3s^23p^3\ ^2D_{5/2}$	···	4.43	2.86	1.81	1.33	1.43	2.10	3.30	4.62	5.91	···
230.79	$3s^23p^2(^3P)3d\ ^2P_{1/2}$	$3s^23p^3\ ^2P_{3/2}$	···	5.02	3.44	2.36	1.86	1.93	2.58	3.75	5.04	···	···

TABLE 1—*Continued*

λ (Å)	Upper Level	Lower Level	$\log[T_e(K)]$										
FeXII *(cont.)*			**5.7**	**5.8**	**5.9**	**6.0**	**6.1**	**6.2**	**6.3**	**6.4**	**6.5**	**6.6**	**6.7**
291.01	$3s3p^4\ ^2P_{3/2}$	$3s^23p^3\ ^2D_{5/2}$	···	4.71	3.18	2.14	1.68	1.80	2.48	3.68	5.00	···	···
335.06	$3s3p^4\ ^2D_{3/2}$	$3s^23p^3\ ^2D_{3/2}$	···	4.90	3.39	2.37	1.93	2.05	2.74	3.95	5.27	···	···
338.26	$3s3p^4\ ^2D_{5/2}$	$3s^23p^3\ ^2D_{5/2}$	···	4.76	3.24	2.22	1.77	1.89	2.58	3.78	5.10	···	···
346.85	$3s3p^4\ ^4P_{1/2}$	$3s^23p^3\ ^4S_{3/2}$	···	4.80	3.26	2.20	1.72	1.80	2.44	3.61	4.89	6.13	···
352.11	$3s3p^4\ ^4P_{3/2}$	$3s^23p^3\ ^4S_{3/2}$	···	4.52	2.98	1.93	1.44	1.52	2.16	3.32	4.60	5.84	···
364.47	$3s3p^4\ ^4P_{5/2}$	$3s^23p^3\ ^4S_{3/2}$	···	4.36	2.82	1.77	1.28	1.36	2.00	3.17	4.44	5.69	···
FeXIII			**5.8**	**5.9**	**6.0**	**6.1**	**6.2**	**6.3**	**6.4**	**6.5**	**6.6**	**6.7**	**6.8**
196.52	$3s^23p3d\ ^1F_3$	$3s^23p^2\ ^1D_2$	6.00	3.79	2.17	1.23	0.91	1.20	2.07	3.09	4.10	5.10	···
200.02	$3s^23p3d\ ^3D_2$	$3s^23p^2\ ^3P_1$	···	3.89	2.29	1.36	1.04	1.34	2.20	3.21	4.22	5.21	···
201.12	$3s^23p3d\ ^3D_1$	$3s^23p^2\ ^3P_1$	5.92	3.74	2.15	1.22	0.90	1.20	2.06	3.08	4.08	5.07	···
202.04	$3s^23p3d\ ^3P_1$	$3s^23p^2\ ^3P_0$	5.63	3.46	1.86	0.94	0.63	0.93	1.80	2.81	3.82	4.80	5.84
202.42	$3s^23p3d\ ^3P_0$	$3s^23p^2\ ^3P_1$	···	4.13	2.54	1.61	1.30	1.59	2.45	3.47	4.47	5.46	···
203.79	$3s^23p3d\ ^3D_2$	$3s^23p^2\ ^3P_2$	5.82	3.64	2.04	1.11	0.79	1.09	1.95	2.97	3.97	4.95	6.00
203.83	$3s^23p3d\ ^3D_3$	$3s^23p^2\ ^3P_2$	5.37	3.18	1.58	0.65	0.33	0.63	1.49	2.50	3.51	4.50	5.54
204.26	$3s^23p3d\ ^1D_2$	$3s^23p^2\ ^3P_1$	···	3.91	2.31	1.38	1.07	1.36	2.23	3.25	4.25	5.25	···
204.94	$3s^23p3d\ ^3D_1$	$3s^23p^2\ ^3P_2$	···	4.20	2.60	1.67	1.36	1.65	2.52	3.53	4.53	5.52	···
209.61	$3s^23p3d\ ^3P_2$	$3s^23p^2\ ^3P_1$	···	3.91	2.32	1.39	1.07	1.37	2.23	3.25	4.26	5.25	···
209.92	$3s^23p3d\ ^3P_1$	$3s^23p^2\ ^3P_2$	···	4.38	2.79	1.86	1.55	1.85	2.72	3.74	4.75	5.73	···
213.77	$3s^23p3d\ ^3P_2$	$3s^23p^2\ ^3P_2$	···	3.94	2.35	1.41	1.10	1.40	2.26	3.28	4.29	5.28	···
216.83	$3s^23p3d\ ^3D_2$	$3s^23p^2\ ^1D_2$	···	4.31	2.71	1.77	1.46	1.75	2.61	3.63	4.63	5.62	···
221.84	$3s^23p3d\ ^1D_2$	$3s^23p^2\ ^1D_2$	···	3.78	2.18	1.25	0.94	1.23	2.10	3.12	4.12	5.12	···
228.16	$3s^23p3d\ ^3P_2$	$3s^23p^2\ ^1D_2$	···	3.99	2.39	1.46	1.15	1.45	2.31	3.33	4.34	5.33	···
240.71	$3s3p^3\ ^3S_1$	$3s^23p^2\ ^3P_0$	···	4.20	2.62	1.70	1.39	1.69	2.56	3.58	4.59	5.58	···
246.21	$3s3p^3\ ^3S_1$	$3s^23p^2\ ^3P_1$	5.97	3.80	2.22	1.30	0.99	1.29	2.16	3.18	4.19	5.18	···
251.95	$3s3p^3\ ^3S_1$	$3s^23p^2\ ^3P_2$	5.69	3.53	1.95	1.03	0.72	1.02	1.89	2.91	3.92	4.91	5.95
256.42	$3s3p^3\ ^1P_1$	$3s^23p^2\ ^1D_2$	···	4.05	2.46	1.54	1.23	1.53	2.40	3.43	4.44	5.44	···
312.16	$3s3p^3\ ^3P_1$	$3s^23p^2\ ^3P_1$	···	4.41	2.84	1.93	1.63	1.94	2.82	3.85	4.86	5.86	···
313.00	$3s3p^3\ ^3P_0$	$3s^23p^2\ ^3P_1$	···	4.56	3.00	2.09	1.80	2.11	2.99	4.01	5.03	6.02	···
318.21	$3s3p^3\ ^1D_2$	$3s^23p^2\ ^1D_2$	···	4.38	2.80	1.88	1.58	1.89	2.77	3.81	4.83	5.84	···
320.80	$3s3p^3\ ^3P_2$	$3s^23p^2\ ^3P_2$	···	4.00	2.43	1.52	1.22	1.53	2.40	3.42	4.44	5.43	···
348.18	$3s3p^3\ ^3D_1$	$3s^23p^2\ ^3P_0$	···	4.33	2.77	1.87	1.58	1.90	2.78	3.81	4.82	5.81	···
359.63	$3s3p^3\ ^3D_2$	$3s^23p^2\ ^3P_1$	···	4.14	2.59	1.68	1.40	1.71	2.59	3.62	4.63	5.63	···
368.12	$3s3p^3\ ^3D_3$	$3s^23p^2\ ^3P_2$	···	4.12	2.56	1.65	1.35	1.66	2.54	3.57	4.58	5.58	···
FeXIV			**5.9**	**6.0**	**6.1**	**6.2**	**6.3**	**6.4**	**6.5**	**6.6**	**6.7**	**6.8**	**6.9**
211.33	$3s^23d\ ^2D_{3/2}$	$3s^23p\ ^2P_{1/2}$	5.23	3.01	1.55	0.78	0.69	1.20	1.91	2.64	3.37	4.18	5.20
219.13	$3s^23d\ ^2D_{5/2}$	$3s^23p\ ^2P_{3/2}$	5.32	3.10	1.64	0.88	0.78	1.29	2.02	2.75	3.49	4.32	5.36
220.10	$3s^23d\ ^2D_{3/2}$	$3s^23p\ ^2P_{3/2}$	5.90	3.68	2.22	1.46	1.36	1.87	2.59	3.31	4.04	4.85	5.87
252.19	$3s3p^2\ ^2P_{3/2}$	$3s^23p\ ^2P_{1/2}$	5.83	3.63	2.18	1.42	1.34	1.85	2.58	3.31	4.06	4.88	5.92
257.38	$3s3p^2\ ^2P_{1/2}$	$3s^23p\ ^2P_{1/2}$	5.61	3.42	1.98	1.23	1.15	1.67	2.40	3.13	3.88	4.70	5.73
264.78	$3s3p^2\ ^2P_{3/2}$	$3s^23p\ ^2P_{3/2}$	5.21	3.01	1.56	0.80	0.71	1.23	1.96	2.69	3.44	4.26	5.30
270.51	$3s3p^2\ ^2P_{1/2}$	$3s^23p\ ^2P_{3/2}$	5.48	3.29	1.85	1.10	1.02	1.54	2.27	3.00	3.75	4.57	5.60
274.20	$3s3p^2\ ^2S_{1/2}$	$3s^23p\ ^2P_{1/2}$	5.67	3.46	2.00	1.22	1.12	1.63	2.35	3.07	3.81	4.62	5.64
334.18	$3s3p^2\ ^2D_{3/2}$	$3s^23p\ ^2P_{1/2}$	5.79	3.60	2.16	1.40	1.32	1.84	2.56	3.29	4.04	4.85	5.88
353.84	$3s3p^2\ ^2D_{5/2}$	$3s^23p\ ^2P_{3/2}$	5.93	3.76	2.32	1.58	1.50	2.03	2.77	3.51	4.27	5.11	6.16
FeXV			**6.0**	**6.1**	**6.2**	**6.3**	**6.4**	**6.5**	**6.6**	**6.7**	**6.8**	**6.9**	**7.0**
233.87	$3s3d\ ^3D_3$	$3s3p\ ^3P_2$	5.59	3.55	2.29	1.77	1.93	2.34	2.81	3.32	3.94	4.81	5.99
243.80	$3s3d\ ^1D_2$	$3s3p\ ^1P_1$	5.15	3.08	1.79	1.24	1.35	1.73	2.15	2.62	3.20	4.02	5.15
284.15	$3s3p\ ^1P_1$	$3s^2\ ^1S_0$	3.87	1.84	0.58	0.05	0.18	0.56	0.99	1.45	2.03	2.84	3.96
305.00	$3p^2\ ^3P_2$	$3s3p\ ^3P_2$	5.76	3.73	2.48	1.96	2.11	2.52	2.98	3.49	4.10	4.95	6.12
321.82	$3p^2\ ^3P_1$	$3s3p\ ^3P_2$	···	4.24	3.00	2.49	2.66	3.08	3.55	4.08	4.70	5.57	···
327.03	$3p^2\ ^1D_2$	$3s3p\ ^3P_2$	5.89	3.85	2.59	2.06	2.20	2.60	3.04	3.53	4.12	4.96	6.11
393.98	$3s3p\ ^3P_2$	$3s^2\ ^1S_0$	···	4.91	3.65	3.12	3.26	3.65	4.10	4.58	5.18	6.01	···
417.24	$3s3p\ ^3P_1$	$3s^2\ ^1S_0$	5.34	3.33	2.08	1.57	1.72	2.13	2.58	3.08	3.68	4.53	5.68
FeXVI			**6.1**	**6.2**	**6.3**	**6.4**	**6.5**	**6.6**	**6.7**	**6.8**	**6.9**	**7.0**	**7.1**
251.05	$2p^63d\ ^2D_{3/2}$	$2p^63p\ ^2P_{1/2}$	4.82	2.98	1.97	1.70	1.76	1.91	2.14	2.51	3.12	4.07	5.37
262.97	$2p^63d\ ^2D_{5/2}$	$2p^63p\ ^2P_{3/2}$	4.60	2.76	1.75	1.48	1.53	1.68	1.92	2.28	2.90	3.85	5.14
265.01	$2p^63d\ ^2D_{3/2}$	$2p^63p\ ^2P_{3/2}$	5.61	3.77	2.76	2.50	2.55	2.70	2.94	3.30	3.92	4.87	···
335.41	$2p^63p\ ^2P_{3/2}$	$2p^63s\ ^2S_{1/2}$	3.35	1.55	0.57	0.33	0.40	0.56	0.81	1.17	1.79	2.74	4.03
360.80	$2p^63p\ ^2P_{1/2}$	$2p^63s\ ^2S_{1/2}$	3.68	1.88	0.90	0.66	0.73	0.89	1.14	1.50	2.12	3.07	4.36

TABLE 1—*Continued*

λ (Å)	Upper Level	Lower Level	$log[T_e(K)]$										
FeXVII			**6.2**	**6.3**	**6.4**	**6.5**	**6.6**	**6.7**	**6.8**	**6.9**	**7.0**	**7.1**	**7.2**
204.65	$2p^5 3p\ ^1S_0$	$2p^5 3s\ ^3P_1$	5.77	4.04	3.20	2.78	2.52	2.40	2.46	2.80	3.51	4.57	5.97
254.87	$2p^5 3p\ ^1S_0$	$2p^5 3s\ ^1P_1$	5.83	4.10	3.27	2.84	2.59	2.47	2.52	2.86	3.57	4.63	6.03
323.56	$2p^5 3p\ ^3P_2$	$2p^5 3s\ ^3P_2$	···	4.77	3.97	3.56	3.32	3.21	3.27	3.62	4.34	5.43	···
340.40	$2p^5 3p\ ^3P_2$	$2p^5 3s\ ^3P_1$	···	4.84	4.04	3.64	3.40	3.28	3.34	3.70	4.42	5.51	···
347.85	$2p^5 3p\ ^1D_2$	$2p^5 3s\ ^1P_1$	···	4.61	3.80	3.39	3.14	3.02	3.08	3.43	4.14	5.23	···
350.50	$2p^5 3p\ ^3D_3$	$2p^5 3s\ ^3P_2$	6.01	4.33	3.53	3.14	2.91	2.81	2.88	3.25	3.99	5.10	···
351.55	$2p^5 3p\ ^3P_1$	$2p^5 3s\ ^1P_1$	···	4.70	3.90	3.50	3.27	3.16	3.22	3.59	4.32	5.42	···
367.26	$2p^5 3p\ ^3D_2$	$2p^5 3s\ ^3P_2$	···	4.74	3.97	3.59	3.37	3.27	3.33	3.70	4.42	5.52	···
373.41	$2p^5 3p\ ^3D_1$	$2p^5 3s\ ^3P_0$	···	4.66	3.92	3.57	3.38	3.30	3.37	3.74	4.47	5.58	···
389.08	$2p^5 3p\ ^3D_2$	$2p^5 3s\ ^3P_1$	···	4.67	3.90	3.52	3.31	3.21	3.27	3.63	4.35	5.45	···
409.69	$2p^5 3p\ ^3S_1$	$2p^5 3s\ ^3P_2$	6.21	4.53	3.73	3.33	3.10	3.00	3.06	3.43	4.16	5.27	···
FeXVIII			**6.3**	**6.4**	**6.5**	**6.6**	**6.7**	**6.8**	**6.9**	**7.0**	**7.1**	**7.2**	**7.3**
93.92	$2s2p^6\ ^2S_{1/2}$	$2p^5\ ^2P_{3/2}$	4.15	3.01	2.33	1.86	1.54	1.40	1.57	2.10	3.00	4.22	5.58
103.94	$2s2p^6\ ^2S_{1/2}$	$2p^5\ ^2P_{1/2}$	4.63	3.48	2.80	2.33	2.02	1.88	2.04	2.58	3.48	4.70	···
FeXIX			**6.4**	**6.5**	**6.6**	**6.7**	**6.8**	**6.9**	**7.0**	**7.1**	**7.2**	**7.3**	**7.4**
78.90	$2s2p^5\ ^1P_1$	$2s^2 2p^4\ ^3P_2$	···	···	4.72	4.00	3.52	3.37	3.64	4.30	5.30	···	···
83.40	$2s2p^5\ ^1P_1$	$2s^2 2p^4\ ^3P_1$	···	···	···	5.16	4.68	4.53	4.80	5.46	···	···	···
83.89	$2s2p^5\ ^1P_1$	$2s^2 2p^4\ ^3P_0$	···	···	···	4.94	4.46	4.31	4.58	5.24	···	···	···
91.02	$2s2p^5\ ^1P_1$	$2s^2 2p^4\ ^1D_2$	···	4.68	3.72	3.00	2.52	2.38	2.65	3.31	4.30	5.46	···
101.55	$2s2p^5\ ^3P_1$	$2s^2 2p^4\ ^3P_2$	5.35	4.09	3.14	2.43	1.95	1.80	2.07	2.73	3.73	4.88	···
106.12	$2s2p^5\ ^1P_1$	$2s^2 2p^4\ ^1S_0$	···	···	4.92	4.20	3.72	3.58	3.84	4.51	5.50	···	···
106.33	$2s2p^5\ ^3P_0$	$2s^2 2p^4\ ^3P_1$	···	···	···	5.15	4.70	4.59	4.90	5.60	···	···	···
108.37	$2s2p^5\ ^3P_2$	$2s^2 2p^4\ ^3P_2$	4.92	3.67	2.72	2.02	1.54	1.40	1.67	2.34	3.33	4.49	5.64
109.97	$2s2p^5\ ^3P_1$	$2s^2 2p^4\ ^3P_0$	5.69	4.43	3.48	2.76	2.28	2.14	2.41	3.07	4.06	5.22	···
111.70	$2s2p^5\ ^3P_1$	$2s^2 2p^4\ ^3P_1$	···	4.54	3.59	2.87	2.39	2.25	2.52	3.18	4.17	5.33	···
120.00	$2s2p^5\ ^3P_2$	$2s^2 2p^4\ ^3P_1$	5.54	4.29	3.34	2.63	2.16	2.02	2.29	2.96	3.95	5.11	···
132.63	$2s2p^5\ ^3P_2$	$2s^2 2p^4\ ^1D_2$	···	4.99	4.04	3.33	2.86	2.72	2.99	3.65	4.65	5.81	···
149.00	$2s2p^5\ ^3P_1$	$2s^2 2p^4\ ^1S_0$	···	5.85	4.90	4.18	3.70	3.56	3.83	4.49	5.48	···	···
424.26	$2s^2 2p^4\ ^1S_0$	$2s^2 2p^4\ ^3P_1$	···	5.87	4.94	4.25	3.78	3.65	3.93	4.60	5.59	···	···
592.20	$2s^2 2p^4\ ^1D_2$	$2s^2 2p^4\ ^3P_2$	6.15	4.92	3.99	3.28	2.79	2.60	2.81	3.40	4.33	5.44	···
FeXX			**6.5**	**6.6**	**6.7**	**6.8**	**6.9**	**7.0**	**7.1**	**7.2**	**7.3**	**7.4**	**7.5**
110.63	$2s2p^4\ ^2D_{3/2}$	$2s^2 2p^3\ ^2D_{3/2}$	···	5.14	3.97	3.11	2.64	2.63	3.03	3.79	4.73	5.69	···
118.66	$2s2p^4\ ^4P_{1/2}$	$2s^2 2p^3\ ^4S_{3/2}$	5.65	4.16	2.99	2.14	1.67	1.66	2.07	2.82	3.77	4.73	5.65
121.83	$2s2p^4\ ^4P_{3/2}$	$2s^2 2p^3\ ^4S_{3/2}$	5.37	3.88	2.71	1.86	1.39	1.38	1.78	2.54	3.49	4.45	5.37
132.85	$2s2p^4\ ^4P_{5/2}$	$2s^2 2p^3\ ^4S_{3/2}$	5.28	3.79	2.62	1.77	1.30	1.30	1.70	2.46	3.41	4.37	5.29
FeXXI			**6.6**	**6.7**	**6.8**	**6.9**	**7.0**	**7.1**	**7.2**	**7.3**	**7.4**	**7.5**	**7.6**
91.28	$2s2p^3\ ^3S_1$	$2s^2 2p^2\ ^3P_0$	···	4.97	3.71	2.89	2.57	2.71	3.23	3.95	4.71	5.45	···
97.88	$2s2p^3\ ^3S_1$	$2s^2 2p^2\ ^3P_1$	···	4.58	3.31	2.50	2.17	2.32	2.84	3.56	4.32	5.05	···
102.22	$2s2p^3\ ^3S_1$	$2s^2 2p^2\ ^3P_2$	···	4.21	2.95	2.13	1.81	1.95	2.47	3.19	3.95	4.69	5.40
108.12	$2s2p^3\ ^3P_1$	$2s^2 2p^2\ ^3P_0$	···	4.91	3.65	2.84	2.51	2.66	3.17	3.89	4.65	5.38	···
113.30	$2s2p^3\ ^1D_2$	$2s^2 2p^2\ ^1D_2$	···	···	4.87	4.09	3.80	3.99	4.55	5.31	···	···	···
117.51	$2s2p^3\ ^3P_1$	$2s^2 2p^2\ ^3P_1$	···	4.35	3.08	2.27	1.94	2.09	2.61	3.33	4.09	4.82	5.53
121.21	$2s2p^3\ ^3P_2$	$2s^2 2p^2\ ^3P_2$	···	···	4.59	3.83	3.54	3.73	4.28	5.04	···	···	···
123.83	$2s2p^3\ ^3P_1$	$2s^2 2p^2\ ^3P_2$	···	5.09	3.83	3.02	2.69	2.84	3.36	4.07	4.83	5.56	···
128.73	$2s2p^3\ ^3D_1$	$2s^2 2p^2\ ^3P_0$	5.18	3.54	2.28	1.47	1.15	1.30	1.83	2.55	3.32	4.05	4.77
142.16	$2s2p^3\ ^3D_2$	$2s^2 2p^2\ ^3P_1$	···	5.37	4.16	3.40	3.13	3.34	3.92	4.69	5.52	···	···
142.27	$2s2p^3\ ^3D_1$	$2s^2 2p^2\ ^3P_1$	···	4.76	3.50	2.70	2.38	2.53	3.05	3.78	4.54	5.28	···
145.65	$2s2p^3\ ^3D_3$	$2s^2 2p^2\ ^3P_2$	···	5.46	4.30	3.60	3.37	3.61	4.21	5.02	5.87	···	···
148.79	$2s2p^3\ ^3P_1$	$2s^2 2p^2\ ^1D_2$	···	···	4.94	4.13	3.80	3.95	4.46	5.18	···	···	···
151.63	$2s2p^3\ ^3D_1$	$2s^2 2p^2\ ^3P_2$	···	5.82	4.56	3.76	3.44	3.59	4.11	4.84	5.60	···	···
189.81	$2s2p^3\ ^3D_1$	$2s^2 2p^2\ ^1D_2$	···	5.48	4.22	3.42	3.10	3.25	3.77	4.50	5.26	···	···
242.07	$2s2p^3\ ^3D_1$	$2s^2 2p^2\ ^1S_0$	···	···	4.88	4.08	3.76	3.91	4.43	5.16	5.92	···	···
251.00	$2s2p^3\ ^5S_2$	$2s^2 2p^2\ ^3P_1$	···	5.79	4.59	3.84	3.57	3.78	4.36	5.15	5.97	···	···
270.52	$2s2p^3\ ^5S_2$	$2s^2 2p^2\ ^3P_2$	···	5.85	4.65	3.90	3.63	3.84	4.42	5.20	6.03	···	···
335.90	$2s^2 2p^2\ ^1S_0$	$2s^2 2p^2\ ^3P_1$	···	5.73	4.51	3.75	3.46	3.64	4.19	4.94	5.72	···	···
587.90	$2s^2 2p^2\ ^1D_2$	$2s^2 2p^2\ ^3P_1$	···	5.77	4.56	3.79	3.50	3.69	4.24	4.99	5.78	···	···

TABLE 1—*Continued*

λ (Å)	Upper Level	Lower Level	$log[T_e(K)]$										
FeXXII			**6.8**	**6.9**	**7.0**	**7.1**	**7.2**	**7.3**	**7.4**	**7.5**	**7.6**	**7.7**	**7.8**
100.78	$2s2p^2\ ^2P_{3/2}$	$2s^22p\ ^2P_{1/2}$	4.72	3.52	2.88	2.75	3.01	3.51	4.05	4.59	5.13	5.66	...
114.41	$2s2p^2\ ^2P_{3/2}$	$2s^22p\ ^2P_{3/2}$	3.91	2.72	2.08	1.94	2.21	2.70	3.24	3.79	4.32	4.85	5.40
116.28	$2s2p^2\ ^2P_{1/2}$	$2s^22p\ ^2P_{3/2}$	4.52	3.33	2.69	2.55	2.82	3.31	3.85	4.40	4.93	5.46	...
117.17	$2s2p^2\ ^2S_{1/2}$	$2s^22p\ ^2P_{1/2}$	3.16	1.97	1.33	1.19	1.46	1.96	2.50	3.05	3.58	4.11	4.66
135.78	$2s2p^2\ ^2D_{3/2}$	$2s^22p\ ^2P_{1/2}$	3.21	2.02	1.39	1.25	1.52	2.02	2.56	3.11	3.64	4.17	4.73
155.92	$2s2p^2\ ^2D_{5/2}$	$2s^22p\ ^2P_{3/2}$	5.40	4.25	3.66	3.58	3.90	4.45	5.05	5.67	...	...	...
247.19	$2s2p^2\ ^4P_{1/2}$	$2s^22p\ ^2P_{1/2}$	4.92	3.74	3.12	3.00	3.28	3.79	4.34	4.90	5.44	5.98	...
FeXXIII			**6.8**	**6.9**	**7.0**	**7.1**	**7.2**	**7.3**	**7.4**	**7.5**	**7.6**	**7.7**	**7.8**
132.85	$2s2p\ ^1P_1$	$2s^2\ ^1S_0$	3.97	2.40	1.43	1.01	1.03	1.29	1.63	1.98	2.34	2.70	3.09
263.76	$2s2p\ ^3P_1$	$2s^2\ ^1S_0$	5.33	3.67	2.59	2.06	1.97	2.15	2.42	2.75	3.10	3.49	3.94
FeXXIV			**6.8**	**6.9**	**7.0**	**7.1**	**7.2**	**7.3**	**7.4**	**7.5**	**7.6**	**7.7**	**7.8**
192.04	$2p\ ^2P_{3/2}$	$2s\ ^2S_{1/2}$	5.70	3.71	2.37	1.63	1.37	1.38	1.49	1.63	1.79	1.99	2.21
255.10	$2p\ ^2P_{1/2}$	$2s\ ^2S_{1/2}$	6.07	4.08	2.75	2.02	1.76	1.77	1.88	2.03	2.19	2.38	2.61

only at higher densities; we know of no candidate for blending with the λ204.94 line that would resolve the problem. The observed and predicted values for the Fe XIV λ270.51/λ257.38 ratio differ by roughly a factor of two. If Fe XIV λ257.38 is blended with Ar XIV (noted as an unlikely possibility in the footnote to the catalog), it would make the agreement worse. The Fe XVI observed/predicted ratio for λ251.05/λ265.01 is 2.73; but we note that the λ265.01 line is extremely weak.

For the *EUVE* spectrum of Capella, three ratios appear problematic and require further discussion. The Fe XIX λ109.97/λ101.55 ratio exceeds the predicted value. For the very high density tokamak ($N_e \approx 2.5 \times 10^{13}$ cm^{-3}), the authors presume that the λ109.97 is blended with an Fe XX λ110.63 line that appears at very high density. This line in our model at 10^{13} cm^{-3} could contribute enough to the flux to improve the agreement somewhat (and could bring the ratio into agreement at 10^{14} cm^{-3}). Furthermore there is a problem with the branching ratio of λ101.55/λ111.7. While a blend with λ111.7 might resolve the problem, we note in the next section that it is λ101.55 which is inconsistent with the intensities of the other Fe XIX lines.

Another problem is the Fe XXI λ102.22/λ97.88 ratio. Here we suspect an unidentified blend with the λ97.88 line—a number of other lines are possible between this line and Ne VIII λ98.11—and the wavelength identification seems worse than for other lines. The tokamak data clearly identify λ97.88, separate λ102.22 and λ101.55, and are consistent with the theoretical predictions.

All in all, if we exclude probable blends and weak lines, the data from both cases suggest that the relative transition probabilities are good to better than 35%. We define the figure of merit as the average deviation of $I_{\rm pred}/I_{\rm obs}$. For the set of branching ratios listed in Table 3, excluding known blends, the average deviation is ~35%. We note that if either plasma had substantial optical depth in Fe resonance lines (e.g., Waljeski et al. 1994), we might see a weakening of these lines relative to transitions which terminate in excited levels. There is no indication of a systematic weakness of the lines expected to be reduced by resonant scattering; therefore, the optical depth is small.

3.2. *Intensity Comparisons for Each Ion*

For a coronal plasma, comparison among line intensities for a particular stage of ionization essentially reflects their collisional excitation processes. For the simplest case of two lines both excited from a single ground-state level, the ratio is simply the ratio of the collisional rates. The purest example found in both spectra is the ratio of the transitions from the Fe XVI $2p^63s\ ^2S_{1/2}$ ground to the $2p^63p\ ^2P_{1/2}$ and $^2P_{3/2}$ levels—the λ335.41/λ360.80 line ratio (Model: 1.98; SERTS: 2.23; *EUVE* Capella: 1.99). For these particular lines, the collision strengths show the same variation with temperature over the interesting range. In general, of course, effective collision strengths show individual variations with temperature. Resonance effects near the threshold energy are specific to the particular transition, but the higher energy behavior follows typical patterns for the type of transition (allowed, intersystem, forbidden). The considerable complexity caused by multiplet ground states and low-lying metastable levels makes the simple interpretation of these relative intensities based on excitation rate ratios unreliable. If the available density-sensitive line ratios were in good agreement as to the value of the density, even for a single ionization state, the task would be simplified; unfortunately, there is considerable spread (see § 4). Thus before constructing an emission measure distribution based on individual line intensities, it is necessary to develop some judgment about the suitability of particular lines for this process. As a particularly difficult example, Fe XIII is a complex ion formed just above 10^6 K, with 37 candidate lines in the SERTS spectrum. Of the 25 lines included in Table 1 (selected on the basis of intensity), all 25 made it to Table 2 based on the 20% variation criterion. Thus in this section we discuss the process of establishing credible candidates for emission measure analysis.

Since the two data sets are mutually exclusive with respect to comparisons within a single ionization stage (except for the

TABLE 2

ELECTRON DENSITY SCALING FOR LINE EMISSIVITIES[a]

Ion	λ (Å)	N_e (cm^{-3})				
		10^8	10^9	10^{11}	10^{12}	10^{13}
Fe IX	171.07	1.304	1.251	0.661	0.580	0.571
	230.52	9.444	5.889	0.090	0.008	0.001
	241.74	1.937	1.675	0.185	0.018	0.002
	244.91	0.916	1.011	0.860	0.797	0.789
Fe X	170.58	0.219	0.397	1.339	1.393	1.393
	174.53	1.404	1.311	0.816	0.789	0.785
	175.27	0.218	0.397	1.336	1.389	1.394
	175.47	0.509	0.621	1.208	1.242	1.245
	177.24	1.370	1.288	0.829	0.803	0.801
	180.41	0.508	0.621	1.209	1.244	1.244
	182.31	1.372	1.283	0.827	0.802	0.798
	184.54	1.240	1.188	0.889	0.875	0.870
	190.04	1.240	1.187	0.887	0.871	0.869
	225.29	0.782	0.841	0.965	0.920	0.914
	257.30	2.647	2.294	0.140	0.014	0.001
Fe XI	178.10	0.502	0.704	0.619	0.381	0.334
	179.76	0.053	0.214	1.200	0.919	0.847
	180.40	1.832	1.620	0.433	0.256	0.225
	180.60	0.634	0.851	0.608	0.380	0.335
	181.10	0.635	0.850	0.609	0.381	0.337
	182.20	0.502	0.707	0.621	0.381	0.335
	184.70	1.124	1.144	0.558	0.350	0.309
	184.80	0.064	0.255	1.103	0.825	0.759
	188.22	1.636	1.483	0.461	0.275	0.241
	189.02	0.058	0.404	0.667	0.410	0.360
	189.10	1.123	1.144	0.557	0.350	0.308
	189.70	1.125	1.145	0.557	0.349	0.309
	192.02	1.478	1.380	0.485	0.291	0.256
	192.82	1.636	1.486	0.462	0.275	0.242
	201.74	1.481	1.382	0.485	0.292	0.256
	204.60	0.275	0.438	1.023	0.768	0.706
	352.68	1.488	1.379	0.486	0.288	0.251
Fe XII	186.86	0.109	0.179	3.668	4.912	5.044
	186.88	0.228	0.607	1.434	1.594	1.623
	188.17	0.051	0.144	3.131	4.000	4.117
	190.06	1.191	1.142	0.766	0.667	0.654
	191.04	0.089	0.323	1.578	1.740	1.770
	192.39	1.360	1.230	0.647	0.508	0.489
	193.51	1.423	1.285	0.577	0.412	0.390
	195.12	1.430	1.291	0.572	0.406	0.383
	195.19	0.051	0.293	1.625	1.815	1.840
	196.64	0.204	0.571	1.514	1.706	1.733
	201.12	0.084	0.221	3.142	4.082	4.209
	203.27	0.619	0.818	1.195	1.267	1.275
	206.37	1.189	1.136	0.762	0.665	0.650
	211.74	1.138	1.072	0.831	0.756	0.746
	217.27	0.306	0.603	1.399	1.541	1.554
	219.44	0.307	0.606	1.401	1.543	1.560
	230.79	1.140	1.078	0.829	0.759	0.749
	291.01	0.379	0.640	1.496	1.686	1.711
	335.06	0.121	0.336	1.736	1.981	2.019
	338.26	0.307	0.596	1.626	1.878	1.913
	346.85	1.400	1.264	0.623	0.479	0.460
	352.11	1.389	1.258	0.632	0.491	0.472
	364.47	1.384	1.255	0.638	0.499	0.480
Fe XIII	196.52	0.035	0.208	1.994	2.270	2.301
	200.02	0.138	0.682	0.942	0.901	0.893
	201.12	0.661	0.972	0.862	0.801	0.790
	202.04	5.707	2.916	0.675	0.618	0.613
	202.42	0.198	0.843	0.862	0.792	0.780
	203.79	0.138	0.680	0.940	0.895	0.887
Fe XIII *(Cont.)*	203.83	0.123	0.645	0.895	0.842	0.834
	204.26	0.150	0.652	1.210	1.244	1.245
	204.94	0.660	0.970	0.859	0.798	0.787
	209.61	0.146	0.659	1.070	1.066	1.063
	209.92	5.678	2.907	0.674	0.619	0.610
	213.77	0.146	0.660	1.071	1.066	1.063
	216.83	0.138	0.683	0.941	0.901	0.891
	221.84	0.150	0.654	1.214	1.252	1.252
	228.16	0.146	0.659	1.072	1.068	1.065
	240.71	1.084	1.086	0.845	0.789	0.779
	246.21	1.079	1.079	0.841	0.784	0.775
	251.95	1.083	1.083	0.845	0.788	0.777
	256.42	0.508	0.600	1.633	1.891	1.924
	312.16	2.386	1.635	0.795	0.741	0.734
	318.21	0.101	0.254	1.970	2.232	2.265
	320.80	0.142	0.674	0.881	0.826	0.817
	348.18	5.123	2.704	0.704	0.649	0.641
	359.63	0.269	0.859	0.870	0.804	0.791
	368.12	0.122	0.634	0.921	0.876	0.868
Fe XIV	211.33	1.597	1.455	0.750	0.710	0.710
	219.13	0.067	0.287	1.384	1.445	1.445
	220.10	1.604	1.463	0.753	0.715	0.712
	252.19	0.612	0.704	1.162	1.186	1.188
	257.38	1.320	1.244	0.868	0.849	0.846
	264.78	0.612	0.704	1.155	1.180	1.184
	270.51	1.314	1.238	0.864	0.845	0.843
	274.20	1.432	1.336	0.819	0.793	0.789
	334.18	1.664	1.507	0.726	0.686	0.681
	353.84	0.145	0.347	1.356	1.407	1.412
Fe XV	233.87	0.314	0.433	1.516	1.610	1.623
	305.00	0.299	0.420	1.526	1.628	1.635
Fe XIX	106.33	0.677	0.797	2.182	13.364	89.455
Fe XXI	91.28	0.998	0.998	1.025	1.146	1.337
	97.88	1.000	1.000	1.023	1.147	1.336
	102.22	0.998	0.998	1.020	1.148	1.334
	113.30	0.869	0.882	2.111	9.361	27.500
	121.21	0.642	0.675	4.094	23.309	53.022
	128.73	1.003	1.003	0.970	0.781	0.391
	142.16	0.957	0.960	1.374	4.167	13.548
	142.27	1.004	1.004	0.971	0.780	0.390
	145.65	0.850	0.866	2.261	10.119	22.451
	151.63	1.000	1.000	0.969	0.780	0.390
	180.55	0.851	0.864	2.264	10.131	22.480
	189.81	1.003	1.003	0.970	0.782	0.390
	242.07	1.000	1.000	0.971	0.784	0.390
	251.00	0.996	0.996	1.019	1.144	1.415
	270.52	1.000	1.000	1.020	1.146	1.417
	335.90	1.000	1.000	1.009	1.071	1.382
	587.90	0.984	0.985	1.146	2.051	3.266
Fe XXII	100.78	0.999	0.999	1.007	1.077	1.623
	114.41	0.998	0.998	1.006	1.076	1.619
	116.28	0.992	0.992	1.008	1.136	2.129
	155.92	0.976	0.982	1.180	2.952	16.826

[a] Scaling factors are given relative to the emissivities in Table 1 for $N_e = 10^{10}$ cm^{-3}. To compute a line's emissivity at a given density, multiply P_λ from Table 1 by the scaling factor in Table 2.

TABLE 3

COMPARISON OF BRANCHING RATIOS

Ion	λ_1	λ_2	Intensity[λ_1]/Intensity[λ_2][a]			
			Model	SERTS[b]	Full Sun[c]	Full Sun[d]
Fe X	345.75	365.57	2.26	1.67 ± 0.32	11.0	···
Fe XI	341.11	356.55	1.87	2.38 ± 0.86	1.5	···
Fe XI	341.11	358.64	1.47	0.49 ± 0.10	1.8	···
Fe XI	352.68	369.23	4.09	3.28 ± 0.59	3.3[e]	···
Fe XI	352.68	406.84[f]	66.5	38.90 ±15.43	···	···
Fe XII	338.26	382.83	4.72	9.53 ± 3.10	···	···
Fe XIII	201.12	204.94	2.80[g]	1.11 ± 0.49[e]	3.2[e]	3.7
Fe XIII	209.61	213.77	1.05	1.58 ± 1.14	0.9	···
Fe XIII	221.84	204.26	1.47	1.17 ± 0.50	···	···
Fe XIII	251.95	240.71	4.89	2.57 ± 1.13	2.0[e]	2.2
Fe XIII	251.95	246.21	1.92	2.33 ± 0.78	2.0	1.7
Fe XIII	312.16	321.45	2.05	2.54 ± 0.68	···	···
Fe XIII	320.80	311.55	7.14	4.34 ± 1.29	3.5	···
Fe XIII	348.18	359.84	3.78	5.53 ± 1.27	5.0	···
Fe XIII	368.12	412.98	13.5	16.50 ± 5.31[e]	···	···
Fe XIV	211.33	220.10	4.51	3.87 ± 0.91	2.2	3.5
Fe XIV	264.78	252.19	4.38	5.75 ± 1.91	4.2	4.0[e]
Fe XIV	270.51	257.38	1.41[h]	2.75 ± 0.64	2.2	···
Fe XIV	274.20	289.16	10.5[h]	13.20 ± 4.35	13.8	15.9
Fe XIV	334.18	356.59	26.0	33.40 ±11.42	···	···
Fe XV	327.03	312.55	1.75	1.38 ± 0.35	···	···
Fe XVI	251.05	265.01	5.89	16.1 ± 9.58	···	···
Fe XVII	389.08	367.26[i]	1.24	1.81 ± 0.99	···	···
			Model	EUVE[j]	PLT[k]	
Fe XVIII	93.92	103.94	2.71	2.59 ± 0.22	2.8	
Fe XIX	108.37	120.00	3.75	3.93 ± 0.52	2.8	
Fe XIX	109.97	101.55	0.50	0.92 ± 0.15	···	
Fe XIX	109.97	111.70	1.27	1.21 ± 0.21	···	
Fe XIX	101.55	111.70	2.54	1.32 ± 0.22	~1.3[l]	
Fe XXI	102.22	97.88	2.42	0.63 ± 0.13	~3.7[l]	

[a] Intensities in photons cm^{-2} s^{-1}.

[b] Thomas & Neupert 1994. Uncertainities given are 1 σ statistical errors. Relative calibration errors are ~20% for first-order lines and ~50% for second-order lines.

[c] Behring et al. 1976.

[d] Malinovsky & Heroux 1973.

[e] Noted by the authors as a blend.

[f] Not identified as Fe XI by Thomas & Neupert.

[g] The tabulated branching ratio is for the Fe XIII lines only. However, in our full model, the blended line Fe XII λ201.12 contributes an additional 3%, 12%, and 44% of the Fe XIII line to the total intensity, for $N_e = 10^9$, 10^{10}, and 10^{11} cm^{-3}, respectively.

[h] For the Fe XIV branching ratio (λ274.20/λ289.16), we have chosen Froese-Fischer & Liu (1986), while other authors give branching ratios of 4.50 (Mason 1975), 3.55 (Bhatia & Kastner 1993) and 15.8 (Huang 1986). Again for Fe XIV, we use Froese-Fischer & Liu 1986 for the branching ratio (λ270.51/λ257.38). Other ratios are 0.82 (Mason 1975), 0.89 (Bhatia & Kastner 1993), and 1.45 (Huang 1986).

[i] Not identified as Fe XVII by Thomas & Neupert.

[j] Observation of Capella; Dupree et al. 1993. Uncertainities given are statistical errors. Relative calibration errors are estimated to be ~10% (Boyd et al. 1994).

[k] Princeton Large Torus (tokamak); Stratton et al. 1985.

[l] One of the lines is weak or poorly separated from another line, increasing the uncertainty to as much as a factor of 2.

Fe XVI lines reported above), we begin with the SERTS spectrum to evaluate Fe IX–XVII and then look at the Capella spectrum for Fe XIX–XXII. In the *EUVE* spectrum, Fe XVIII contributes only the two lines of the branching ratio discussed in the previous section. The observation also includes only one line each for Fe XXIII and Fe XXIV, and both of these lines are blended.

One purpose of this section is to find the "outliers" that we might choose to exclude from further analysis. These "outliers" in general may include undiscovered blends or calibration problems and problems with the atomic rates, as well as potential inapplicability of the model assumptions. For each ionization stage, we construct an emission measure which predicts the intensities of the observed lines, such that log [I_{obs}/

$I_{\rm pred}]_{\rm average} = 0$. For the SERTS spectrum, we have limited the set of observed lines to the first order lines for this purpose.

3.2.1. *SERTS Observations*

Since the overall agreement for all lines is best at $N_e = 10^{10}$ cm^{-3} (within a factor of 10), we have used that density for the average model. Figure 1 and Table 4 (Model 1) present the results for the SERTS spectrum. In addition to the lines listed as Fe, we include two lines identified as Fe XII by Keenan et al. (1995) and four lines listed by Thomas & Neupert (1994) without identifications, which are consistent with the results reported here. We have also computed line intensities at $N_e = 10^9$ and 10^{11} cm^{-3} using the same emission measure distribution. The average deviations for the intensities of a single ion range from about 15% to 50% for the first order lines. If the observed to predicted intensity ratio is not better than a factor of 2 for any density within this range, we make note of the line in the descriptions that follow. We note that the observations for the second-order lines are on average lower than the predictions by approximately 50%. This may be consistent with the 50% relative accuracy for second-order intensities between wavelengths of 188 and 225 Å, as estimated by Thomas & Neupert (1994).

Fe IX.—The λ241.74 and λ244.91 line intensities are consistent with each other to within a factor of 2 at 10^{10} cm^{-3}. Their line ratio indicates an electron density of about 2×10^{10} cm^{-3}. Whereas Feldman (1992, 1993) suggests short-duration bursts or nanoflares during a flare in order to reconcile the densities derived from the λ241.74/λ244.91 intensity ratio with other density diagnostic line ratios, we require no deviation from the equilibrium ionization for the active region spectrum. A "correction" on the order of 50% for λ217.10 brings it into acceptable agreement as well.

The Fe IX λ171.07 is one of the strongest lines in the EUV spectrum of the Sun. Unfortunately, this line falls at the extreme edge of the second order spectrum, for which Thomas & Neupert (1994) do not give an estimate of the calibration uncertainty. Our prediction for λ171.07 exceeds the published value by about a factor of 5. While this discrepancy is disconcerting for such an important spectral landmark, the extrapolated relative calibration error could be as large as a factor of 2–3. As we have noted, the resonance contributions may not be accurately calculated, despite the assertion of Burgess et al. (1993) that the calculations are accurate. An alternative possibility is that Fe IX is not in ionization equilibrium (in the sense that it is excited at a much lower temperature), which might also explain discrepancies with Fe XIV (see below). Since lines of Fe XII that would also exhibit this effect do not, and are in good agreement with the ionization equilibrium, this explanation seems rather arbitrary. Future work on the second-order spectral response curve may improve the agreement for this ion (Thomas 1994).

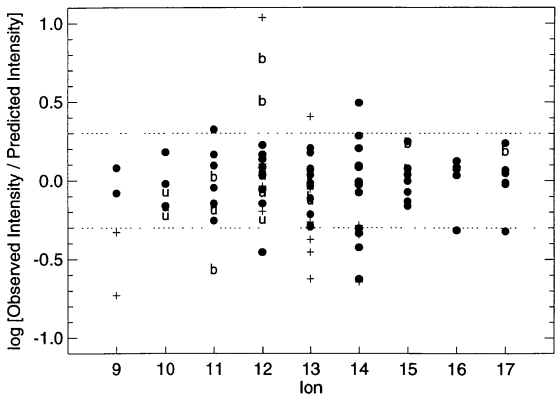

FIG. 1.—Comparison of the observed and predicted intensities for each ionization stage of Fe IX–XVII in the SERTS data. The model assumes $N_e = 10^{10}$ cm^{-3}. The average of the logarithm of the observed-to-predicted intensity ratios for the first-order lines determines the emission measure for that ion. Filled circles = first order; plus signs = second order; b = blend (with a different element or ion); u = upper limit for the observation. The dotted lines represent agreement within a factor of 2 of the average value for that ion.

Fe X.—The ratio of the λ257.3 line to the λλ345.75; 365.57 multiplet is acceptable for the lower density range. This line is a blend of the 257.26 allowed resonance line, and the forbidden λ257.3, which Mason & Nussbaumer (1977) have shown to be a major component. Our prediction is the sum of the two line intensities. The observed second-order line λ174.53 is weaker than the model, even with an adjustment for the presumed calibration difference. This discrepancy is made worse by the fact that it is blended with a first order line of Fe XI (see the next paragraph).

Fe XI.—Except for the λ358.64 branching ratio discussed above, the intensities of this ion agree by our criteria; however, the λ348.97 line is blended with the second-order Fe X λ174.53 line. The λ348.97 alone is consistent in the lower density range; however, the model predicts an additional strong contribution to the observed intensity from the λ174.53 line, using the relative second-order calibration inferred from the reported intensities. Since the observed blend is weak (the uncertainty in its measured intensity is nearly 50%) and since the calibration for λ174.53 is highly uncertain, this discrepancy is perhaps acceptable. We also note that Fe XI λ188.22 is blended with Fe XII λ188.17, which we have added to our intensity prediction.

Fe XII.—Within the density range 10^9–10^{11} cm^{-3}, all of the observed Fe XII lines are predicted to within better than a factor of 2, except for the λ200.36 line.

Fe XIII.—The predictions for the first-order lines observed for this ion are consistent with our criteria for "agreement." As noted above, the branching ratios from the $3s3p^3\,{}^3S_1$ level may be problematic. We note here that the (predicted to be) weaker λ240.71 line is actually more consistent with the other lines observed for this ion, with both λ246.21 and λ251.95 about a factor of 2 too intense. The spread in the second-order lines is significantly larger than for the first-order lines. Within the narrow wavelength range from 195 to 210 Å, for which the relative intensity calibration should not be an issue, the line intensities are not consistent with each other. Again, density-sensitivities complicate the issue.

Fe XIV.—Although four of the five branching ratios agree well with the model, the relative intensities for this ion contain some systematic discrepancies. The quartet system lines are observed to be more than a factor of 3 too large. For the other lines observed, density sensitivity is generous enough to give a factor of 2 agreement for any particular line, but at any single density, several lines are factors of 2–3 different from their predictions.

Fe XV.—The observed lines of Fe XV agree well with the predictions. With such good agreement we would tentatively identify the measured, but unidentified, line in the SERTS spectrum at λ393.97 as the forbidden λ393.98 $3s3p\ ^3P_2$–$3s^2\ ^1S_0$ transition, for which the predicted intensity is consistent within the assumed density range. We do not yet include the $3p3d$ configuration, and thus Fe XV λ372.758, in our predictions; nor do we include λ256.909.

We note that the ratio of the intercombination line to the resonance line (λ417.24)/(λ284.15) marginally agrees with the theoretical prediction, removing the need to appeal to drastic departures from ionization equilibrium (Feldman et al. 1992). Including resonance contributions in the collision strengths would most likely increase the predicted line ratio (Pradhan 1988; Christensen et al. 1985), further improving the agreement. The agreement of the forbidden λ393.98 to resonance line ratio supports the ionization equilibrium model as well. Furthermore, the intensity ratio λ321.82/λ327.03 is also now in excellent agreement with the predictions.

Fe XVI.—Except for the branching ratio noted above, this ion also shows excellent agreement between observation and prediction.

Fe XVII.—The agreement between predictions and observations is excellent. Predictions by Bhatia & Doschek (1992) for the EUV lines agree somewhat less well with the observations than do those of Smith et al. (1985). Since the X-ray lines show discrepancies with respect to theoretical predictions (Rugge & McKenzie 1985; Raymond & Smith 1986; Waljeski et al. 1994), the agreement among the $\Delta n = 0$ ($3s$–$3p$) transitions may help to clarify the issues.

3.2.2. *Capella*

Fe XIX.—The six lines observed in the *EUVE* Capella spectrum for Fe XIX are consistent with predictions, except for the λ101.55 line as noted in the section above. The tokamak group attributes the branching ratio discrepancies to the presence of Fe XX λ110.64 (Stratton et al. 1985). Our resolution is somewhat better, so that we should be able to separate this blend. We do not see a strong λ110.64 line. Since we have good agreement for all the other lines, we would attribute the problem to λ101.55.

Fe XX.—The predicted intensity ratio of λ118.66 to λ121.83 is about 70% of the observed ratio, an acceptable value. The third resonance line from the ^4P multiplet is blended with an Fe XXIII line. We predict the Fe XX contribution to this blend to be about 25%–40%.

Fe XXI.—The observed Fe XXI lines are all density sensitive, and thus it is difficult to establish the problems. As we have stated before, the branching ratio for λ102.22 and λ97.88 is quite discrepant. The λ102.22 line is consistent with the lower density predictions relative to λ128.73. However, the λ97.88, λλ142.16; 142.27, and λ145.65 lines are consistent with the higher densities. Further data may resolve this problem.

Fe XXII.—The intensity ratio of λ135.78/λ117.17 is about 50% low, marginally acceptable. Furthermore, λ135.78 line may be blended with O V, exacerbating the problem. It is also possible that λ117.17 is blended with Fe XXI λ117.51. At the lower densities, the Fe XXI contribution might be roughly one quarter of the line, improving the agreement; at the higher densities, its contribution is negligible.

3.3. *The Emission Measure Distribution Model*

To this point we have compared lines from each species separately. Once the observed lines have been weighted to account for blends, possible calibration errors, potential atomic rate problems, and any other questions, they can be used to determine the emission measure distribution for that species, and, presumably, for a temperature characteristic of that ionization state. Our goal here is twofold: to illustrate the implications of the data selection for the derived emission measure distribution, and, in turn, to use the derived emission measure distributions to verify the atomic models and to identify "outliers."

In this section, we show emission measure distributions from our analysis which are good fits to the comparison observations. We demonstrate that, for high-quality observations, models of the emission measure distribution require a full integration over temperature of all the line emissivities. If the emission measure is much larger at temperatures above an ion's T_{max}, i.e., its temperature of "maximum" ionization fraction, then that ion's emission is weighted toward the higher temperatures. The Capella data dramatically demonstrate this effect. Even for the SERTS data, which fit a smoothly increasing emission measure, significantly more than half the emission for a lower ionization stage such as Fe IX may come from above its T_{max}.

3.3.1. *Method*

We have constructed emission measure distribution models to predict spectral lines for comparison with the observed lines. Specifically, we have adjusted the models in order to minimize the discrepancies, in a manner similar to the method described by Lang et al. (1990). We have included essentially all Fe lines in this analysis, giving more weight to the higher quality observations; in the illustrations that follow we report all observable Fe lines predicted with the derived emission measure distribution. Without knowing a priori which subsets of lines are unambiguous with respect to various uncertainties, this method of constructing models helps to test the atomic models and identify "outliers." We emphasize that the models are quite well constrained, especially at temperatures for which a sufficient number of well-behaved lines exist. Moreover, an emission measure analysis based primarily on the strongest lines, or on lines not sensitive to density, has less success overall with respect to the bulk of the observed lines. In order to analyze the energy balance for these emission regions, of course, statistical tests of the models will be required; however, they must necessarily rely on observations weighted by a number of observational and atomic uncertainties.

3.3.2. *The SERTS Model*

Figure 2 shows the comparison between observations and predictions for the line intensities at their respective wavelengths, calculated using the model emission measure distribution shown by the solid line in Figure 3. The model assumes $N_e = 10^{10}$ cm^{-3} in the solar active region. The results of emission measure distribution modeling for three different densities (including 10^{10}) are also presented in Table 4. The average deviations between observations and predictions for the first order lines range from ~15% to 50% for the various ionization

TABLE 4

COMPARISON OF OBSERVED TO PREDICTED INTENSITIES

Ion	λ (Å)	Ratios of Observed to Predicted Intensities[a]				Observational Uncertainties:		Comments
		Model 1	Model 2a	Model 2b	Model 2c	Statistical	Calibration	
Fe IX	171.07	0.19	0.21	0.26	0.41	31%	...	
Fe IX	217.10	0.47	0.74	0.67	0.67	48%	50%	
Fe IX	241.74	0.83	0.73	1.18	6.27	35%	20%	
Fe IX	244.91	1.20	1.71	1.70	2.04	29%	20%	
Fe X	174.53	0.26	0.22	0.29	0.36	47%	...	Blend with Fe XI λ348.97[b,c]
Fe X	175.27	1.02	2.87	1.14	0.86	...	...	Not observed[d]
Fe X	177.24	0.56	0.50	0.64	0.77	...	...	Not observed[d]
Fe X	184.54	0.79	0.75	0.89	1.00	...	...	Not observed[d]
Fe X	257.26	1.51	0.95	1.70	4.11	25%	20%	Blend with Fe X λ257.3[e]
Fe X	345.75	0.69	0.72	0.78	0.85	12%	20%	
Fe X	365.57	0.95	0.97	1.06	1.15	13%	20%	
Fe XI	188.22	0.99	0.90	1.30	1.88	23%	50%	Blend with Fe XII λ188.17[e]
Fe XI	201.74	0.79	0.72	1.04	2.04	...	50%	Not observed[d]
Fe XI	204.60	0.64	1.87	0.86	0.79	...	50%	Not observed[d]
Fe XI	308.61	1.47	4.35	1.95	1.73	18%	20%	
Fe XI	341.11	0.72	0.74	0.95	1.71	15%	20%	
Fe XI	348.97	0.25	0.77	0.34	0.48	47%	20%	Blend with Fe X λ174.53[f]
Fe XI	352.68	0.72	0.67	0.96	1.88	11%	20%	
Fe XI	356.55	0.56	0.58	0.75	1.35	32%	20%	
Fe XI	358.64	2.12	2.22	2.84	5.11	12%	20%	
Fe XI	369.23	0.90	0.84	1.20	2.35	13%	20%	
Fe XI	406.84	1.25	1.15	1.65	3.22	37%	20%	Our identification
Fe XII	186.88	2.99	4.36	2.85	1.80	24%	...	Blend with S XI; Fe XII λ186.86[e]
Fe XII	191.04	1.47	4.08	1.42	0.82	...	50%	Not observed[d]
Fe XII	192.39	5.57	4.03	5.34	7.62	14%	50%	Blend with Mn XV
Fe XII	193.51	1.14	0.79	1.08	1.73	17%	50%	
Fe XII	195.12	0.64	0.45	0.62	1.01	17%	50%	
Fe XII	196.64	1.28	1.99	1.23	0.74	62%	50%	New addition to the SERTS line list[g]
Fe XII	200.36	10.86	77.83	10.58	2.74	26%	50%	
Fe XII	201.12	0.79	0.79	0.76	0.64	34%	50%	Blend with Fe XIII λ201.12[e,c]
Fe XII	211.74	0.61	0.50	0.59	0.65	...	50%	Not observed[d]
Fe XII	217.27	1.57	2.32	1.52	0.99	...	50%	Not observed[d]
Fe XII	219.44	0.92	1.35	0.88	0.58	44%	50%	
Fe XII	283.64	0.88	2.27	0.85	0.40	50%	20%	New addition to the SERTS line list[g]
Fe XII	291.01	1.68	2.34	1.61	0.98	17%	20%	
Fe XII	305.23	1.50	2.93	1.43	0.52	...	20%	Not observed[d]
Fe XII	335.06	0.35	0.96	0.34	0.18	47%	20%	
Fe XII	338.26	1.47	2.16	1.40	0.79	13%	20%	
Fe XII	346.85	1.09	0.76	1.04	1.55	12%	20%	
Fe XII	352.11	1.22	0.86	1.17	1.72	11%	20%	
Fe XII	364.47	1.37	0.97	1.31	1.91	11%	20%	
Fe XII	382.83	0.72	1.07	0.69	0.39	29%	20%	
Fe XIII	191.23	. . .	. . .	. . .	. . .	47%	...	Blend with S XI[g]
Fe XIII	200.02	0.67	0.77	0.56	0.56	...	50%	Not observed[d]
Fe XIII	201.12	0.90	0.79	0.76	0.64	34%	50%	Blend with Fe XII λ201.12[e]
Fe XIII	202.04	0.88	0.24	0.74	1.03	16%	50%	
Fe XIII	202.42	1.01	0.94	0.85	0.92	...	50%	Not observed[d]
Fe XIII	203.83	0.54	0.65	0.46	0.47	14%	50%	Blend with Fe XIIIλ203.79[e]
Fe XIII	204.26	0.53	0.63	0.44	0.34	29%	50%	
Fe XIII	204.94	2.55	2.06	2.13	2.32	26%	50%	
Fe XIII	208.68	5.70	7.75	4.77	0.78	...	50%	Not observed[d]
Fe XIII	209.61	0.35	0.42	0.30	0.26	54%	50%	
Fe XIII	209.92	1.06	0.28	0.88	1.22	...	50%	Not observed[d]
Fe XIII	213.77	0.24	0.28	0.20	0.17	48%	50%	
Fe XIII	216.83	0.53	0.62	0.45	0.45	...	50%	Not observed,[d] blend with Fe XIII λ216.87[e]
Fe XIII	221.84	0.42	0.50	0.35	0.27	30%	50%	
Fe XIII	240.71	1.16	0.84	0.98	1.09	41%	20%	
Fe XIII	246.21	0.51	0.37	0.42	0.47	30%	20%	
Fe XIII	251.95	0.61	0.44	0.52	0.57	15%	20%	
Fe XIII	256.42	0.73	0.94	0.61	0.35	38%	20%	Blend with Zn XX and Si X

TABLE 4—*Continued*

Ion	λ (Å)	Ratios of Observed to Predicted Intensities[a]				Observational Uncertainties:		Comments
		Model 1	Model 2a	Model 2b	Model 2c	Statistical	Calibration	
Fe XIII	288.75	1.76	2.29	1.47	0.84	···	20%	Not observed[d]
Fe XIII	311.55	1.50	1.77	1.27	1.35	26%	20%	
Fe XIII	312.16	1.19	0.57	1.00	1.17	14%	20%	
Fe XIII	313.00	0.97	0.89	0.81	0.88	28%	20%	Our identification
Fe XIII	318.21	1.19	3.69	1.00	0.47	14%	20%	
Fe XIII	320.80	0.92	1.08	0.77	0.82	12%	20%	
Fe XIII	321.45	0.97	0.46	0.81	0.95	22%	20%	
Fe XIII	348.18	1.61	0.46	1.34	1.77	11%	20%	
Fe XIII	359.63	1.19	1.07	0.99	1.07	11%	20%	
Fe XIII	359.84	1.09	0.32	0.91	1.21	19%	20%	
Fe XIII	368.12	0.92	1.14	0.78	0.79	18%	20%	
Fe XIII	412.98	0.77	0.94	0.64	0.64	26%	20%	
Fe XIII	418.17	1.57	0.46	1.33	1.77	···	20%	Not observed[d]
Fe XIV	211.33	0.45	0.58	0.86	1.12	13%	50%	
Fe XIV	219.13	0.23	1.48	0.44	0.31	15%	50%	
Fe XIV	220.10	0.52	0.67	1.01	1.30	19%	50%	
Fe XIV	252.19	0.38	0.99	0.72	0.60	31%	20%	
Fe XIV	257.38	0.24	0.36	0.46	0.51	19%	20%	
Fe XIV	264.78	0.50	1.30	0.95	0.79	11%	20%	
Fe XIV	270.51	0.46	0.70	0.89	1.00	13%	20%	
Fe XIV	274.20	1.24	1.74	2.40	2.84	11%	20%	
Fe XIV	289.16	0.99	1.39	1.92	2.27	30%	20%	
Fe XIV	334.18	1.22	1.50	2.33	3.12	11%	20%	
Fe XIV	353.84	0.84	4.58	1.63	1.17	11%	20%	
Fe XIV	356.59	0.94	1.17	1.82	2.44	32%	20%	
Fe XIV	429.54	3.13	5.34	6.08	6.20	32%	20%	
Fe XIV	444.26	1.60	2.25	3.09	3.63	22%	20%	
Fe XIV	447.33	1.93	5.35	3.74	3.06	12%	20%	
Fe XV	243.80	0.74	0.83	0.87	0.91	16%	20%	
Fe XV	284.15	0.69	0.77	0.81	0.84	11%	20%	
Fe XV	292.36	1.20	3.28	1.41	0.90	35%	20%	
Fe XV	302.45	0.79	2.98	0.94	0.56	···	20%	Not observed[d]
Fe XV	305.00	1.62	4.45	1.93	1.23	14%	20%	Blend with Mn XIV
Fe XV	312.55	1.09	1.35	1.30	1.24	21%	20%	Blend with Co XVII
Fe XV	321.82	1.00	3.72	1.17	0.70	22%	20%	
Fe XV	327.03	0.85	1.04	1.00	0.95	14%	20%	
Fe XV	393.98	1.77	1.13	2.11	11.67	17%	20%	Our identification
Fe XV	417.24	1.09	1.22	1.28	1.35	11%	20%	
Fe XV	435.20	1.12	3.09	1.33	0.85	···	20%	Not observed[d]
Fe XVI	251.05	1.33	1.20	1.20	1.20	17%	20%	
Fe XVI	262.97	1.19	1.06	1.06	1.06	12%	20%	
Fe XVI	265.01	0.48	0.44	0.44	0.44	56%	20%	
Fe XVI	335.41	1.21	1.09	1.09	1.09	15%	20%	
Fe XVI	360.80	1.08	0.97	0.97	0.97	15%	20%	
Fe XVII	254.87	1.17	1.00	1.00	1.00	48%	20%	
Fe XVII	347.85	1.12	0.96	0.96	0.96	26%	20%	
Fe XVII	350.50	0.95	0.82	0.82	0.82	23%	20%	
Fe XVII	351.55	0.89	0.75	0.75	0.75	···	20%	Not observed[d]
Fe XVII	358.24	1.73	1.50	1.50	1.50	44%	20%	
Fe XVII	367.26	0.97	0.84	0.84	0.84	52%	20%	Our identification
Fe XVII	373.41	0.70	0.60	0.60	0.60	···	20%	Not observed[d]
Fe XVII	387.23	1.00	0.85	0.85	0.85	···	20%	Not observed[d]
Fe XVII	389.08	1.44	1.22	1.22	1.22	17%	20%	Blend with Ar XVI
Fe XVII	409.69	0.48	0.40	0.40	0.40	29%	20%	

[a] Model 1 (shown in Fig. 1) uses the average Emission Measure for the individual ion. $N_e = 10^{10}$ cm^{-3}. Model 2 uses the full Emission Measure Distribution. $N_e = 10^9$, 10^{10}, and 10^{11} cm^{-3} for 2a, 2b (shown in Fig. 2), and 2c, respectively.

[b] Predicted and observed intensities given here for this line only, using the second-order intensities.

[c] This point is not shown for this ion in Figs. 1 and 2, as the contribution from the other ion is predicted to be stronger.

[d] Instead of an observed line intensity we have used the 3 σ intensity limit as an upper limit.

[e] Predicted intensities include both Fe lines in the blend.

[f] Predicted and observed intensities given here for this line only, using the first-order intensities. This ratio is plotted in Figs. 1 and 2 as Fe XI λ348.97.

[g] Reported in Keenan et al. 1995.

[h] Our predicted line intensity is much too weak to contribute to this blend.

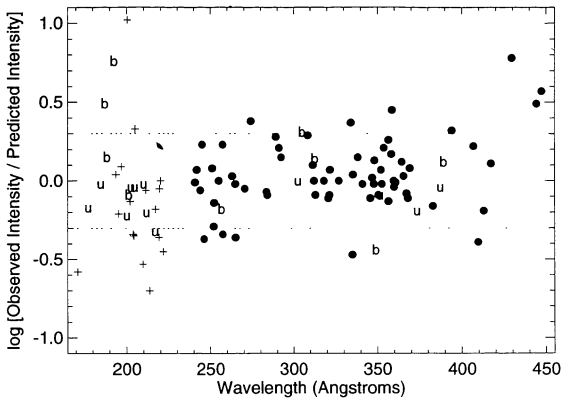

FIG. 2.—Comparison of the observed and predicted intensities for the SERTS data, for the model emission measure distribution, shown vs. wavelength. Again, the model assumes $N_e = 10^{10}$ cm^{-3}. Filled circles = first order; plus signs = second order; b = blend (with a different element or ion); u = upper limit for the observation. Between the dotted lines, agreement is within a factor of 2.

stages, for an overall average deviation of ~35% for first order, and ~50% for both orders. Figure 2 confirms the relative wavelength calibration for first order and suggests that the second order calibration is systematically somewhat low, albeit within the reported uncertainties. The data appear to suggest a problem with the high-wavelength calibration, but atomic rate problems with the Fe XIV quartet system are a more likely explanation.

At some temperatures the emission measure is more constrained than at others, such as where a steep emission measure peaks, or where several ionization stages have peak ionization fractions in a narrow temperature range. The fully integrated emission measure distribution for these cases provides additional information about the uncertainties. As an example, we consider the usefulness of the emission measure model for identifying the Fe IX problem for the SERTS observations. Since more than half the emission in the model comes from above T_{max} [log T_e(K) = 5.8], we fix the emission measure to produce reasonable amounts of Fe X and XI emission, thus determining about half the emission from Fe IX. A requirement for some degree of "smoothness" can be an additional constraint. The results implicate λ171.07 as the most likely of the four lines to be the source of the discrepancy, consistent with the unknown calibration. This example illustrates the power of this technique for testing atomic rates and observations.

It is interesting to consider the "outliers" for ions such as Fe XIII and Fe XIV from the point of view of constraints imposed by the emission measure distribution, as constructed by their adjacent ionization stages. As we have noted, the spread in the observed to predicted ratios for Fe XIV is relatively large; without any information about the emission measure contributing to Fe XIV, it is not possible to distinguish whether the source of discrepancy lies with the intersystem lines or with the interconfiguration transitions (or both). The effect of the emission measure model is to push the lines emitted from the quartet system most out of agreement.

As a second illustration, we can compare our derived emission measure distribution with one that we derive using the Arnaud & Rothenflug (1985) ionization equilibrium, and our collision rates. Requiring the same quality of "fit" using the alternative ionization equilibrium, we construct the emission measure distribution shown by the dotted line in Figure 3. While the slope of the emission measure distribution using Arnaud & Raymond (1992) is more typical of active region models, we claim no definitive test of ionization equilibria.

3.3.3. *The Capella Model*

The solid and dotted curves in Figure 4 show emission measure distributions constructed with our model to fit the Capella spectrum of Dupree et al. (1993). (We have extended the curve to temperatures below those appropriate to our lowest ionization stage by modeling some UV lines with the Raymond & Smith code). In Figure 5 and Table 5 we present the comparison between our predictions and the observations, both at $N_e = 10^{11}$ and 10^{13} cm^{-3}. The average deviation is ~25%.

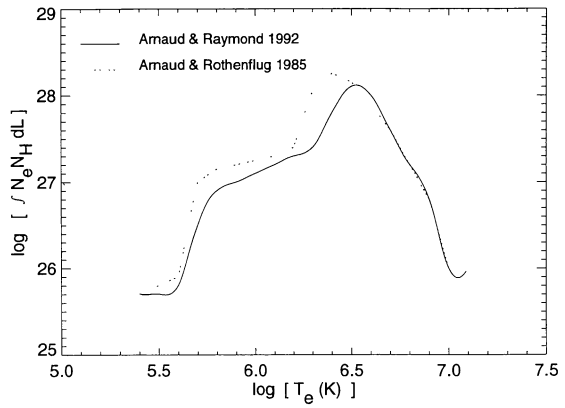

FIG. 3.—Models of the emission measure distributions for the SERTS data. The solid line is the model for $N_e = 10^{10}$ cm^{-3}, assuming the ionization equilibrium of Arnaud & Raymond (1992). The dotted line is the model which assumes the ionization equilibrium of Arnaud & Rothenflug (1985).

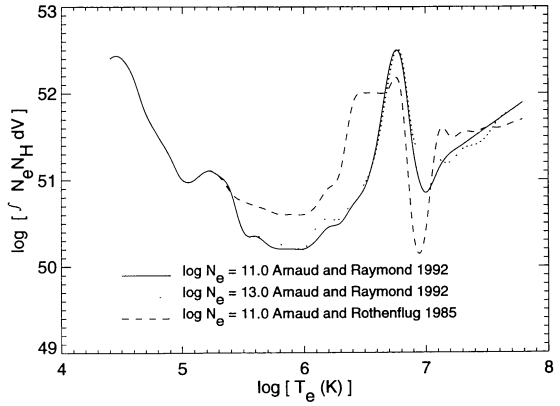

FIG. 4.—Models of the emission measure distributions for the Capella data. The solid line is the model for $N_e = 10^{11}$ cm^{-3}; the dotted line assumes $N_e = 10^{13}$ cm^{-3}—both are for the Arnaud & Raymond (1992) ionization equilibrium. The dashed line is the model for $N_e = 10^{11}$ cm^{-3} with the Arnaud & Rothenflug (1985) ionization equilibrium.

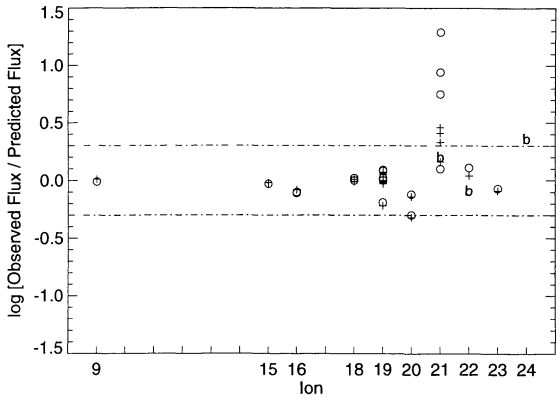

FIG. 5.—Comparison of the observed and predicted fluxes for the Capella data for different densities. ○ = 10^{11} cm^{-3}; + = 10^{13} cm^{-3}; b = blends for 10^{11} cm^{-3} only. Both models shown are for the Arnaud & Raymond (1992) ionization equilibrium.

Dupree et al. have noted the striking features of this distribution: its continuous nature, the minimum at $T_e \approx 10^6$ K, and the "bump" at log $T_e \approx 6.7$. (The minimum at 10^7 K appears necessary for the 10^{13} cm^{-3} model, but is not well constrained.) The authors demonstrate that assigning the emission from lines from each ionization stage to its T_{max} produces an emission measure distribution with similar features. We point out that our modeling method applied to other cases (solar flares observed by *OSO* 5 and HR 1099 data from *EUVE*) lead to continuous plasma distributions without any significant bumps at high temperature.

The high temperature "bump" in the Capella emission measure distribution provides an interesting constraint on the data quality. The emission measure distribution is so steeply peaked at log T_e(K) = 6.7 that the Fe XVIII lines determine in the model the emission from Fe XIX as well. Five of the six Fe XIX lines are in very close agreement with each other and with the Fe XVIII lines, while Fe XIX λ101.55 is about a factor of 2 below the prediction from this model. Thus the emission measure modeling helps to confirm that it is the "outlier" contributing to the branching ratio discrepancies in Table 3.

While Fe XVII has no observed lines in the Capella spectrum, the emission of Fe XVI is substantially derived in the model from the "bump." Approximately 75% of the emission of Fe XVI comes from the narrow range, log T_e = 6.7–6.8, while less than 7% of its emission comes from $\leq T_{max}$. Even for Fe XV, 37% comes from the "bump" temperature range, with only 20% from $\leq T_{max}$. The upshot is that the ratio of Fe XVI/Fe XVIII line intensities is consistent with a single temperature model at the "bump" temperature.

Alternatively, we might ask what emission measure distribution we would construct under different ionization equilibrium models. As an example, the dashed curve in Figure 4 shows the emission measure model derived using Arnaud & Rothenflug (1985). Without the high-temperature tail in the Fe XVI ionization curve found in Arnaud & Raymond (1992), the

TABLE 5

COMPARISON OF OBSERVED TO PREDICTED FLUXES

Ion	λ (Å)	Ratios of Observed to Predicted Fluxes[a]		Observational Uncertainties:		Comments
		10^{11}	10^{13}	Statistical	Calibration	
Fe IX	171.07	0.97	1.03	9%	10%	
Fe XV	284.15	0.94	0.95	8%	10%	
Fe XVI	335.41	0.79	0.83	5%	10%	
Fe XVI	360.80	0.78	0.83	8%	10%	
Fe XVIII	93.92	1.00	0.97	5%	10%	
Fe XVIII	103.94	1.05	1.01	7%	10%	
Fe XIX	91.02	1.05	0.94	17%	10%	
Fe XIX	101.55	0.65	0.61	11%	10%	
Fe XIX	108.37	1.04	1.00	5%	10%	
Fe XIX	109.97	1.19	1.11	12%	10%	
Fe XIX	111.70	1.24	1.16	13%	10%	
Fe XIX	120.00	0.99	0.95	12%	10%	
Fe XX	118.66	0.75	0.72	13%	10%	
Fe XX	121.83	0.51	0.48	12%	10%	
Fe XXI	97.88	5.57	2.89	13%	10%	
Fe XXI	102.22	1.45	0.75	16%	10%	Blend with O VIII
Fe XXI	128.73	1.27	2.16	10%	10%	
Fe XXI	142.27	8.64	2.55	17%	10%	
Fe XXI	145.65	19.53	1.45	25%	10%	
Fe XXII	117.17	1.30	1.11	10%	10%	
Fe XXII	135.78	0.74	0.63	17%	10%	Blend with O V
Fe XXIII	132.85	0.85	0.81	7%	10%	Blend with Fe XX λ132.85[b]
Fe XXIV	192.04	2.07	2.26	8%	10%	Blend with O V and Ca XVII

[a] Models for these two N_e [cm^{-3}] cases are also shown in Fig. 5.

[b] Predicted flux is the sum of both line intensities; and therefore, Fig. 5 does not represent this line as a blend. The ratios are plotted in Fig. 5 at Fe XXIII, since that contribution dominates in the models.

"bump" significantly broadens and a deep minimum at 10^7 K is required. Nevertheless, the basic features of Dupree et al. are still maintained.

4. DISCUSSION OF DENSITY DIAGNOSTICS

Both observations contain useful pairs of lines for determining the electron density of the emitting plasma. As Dupree et al. (1993) have discussed for Capella, the spread in the indicated electron density by different line ratios is disturbingly large. The SERTS spectrum also shows a wide range of densities depending on the particular diagnostic ratio, even for the same ionization stage. The SERTS spectrum, with its large sets of lines for various ionization stages, provides an opportunity to determine sources of the spread in derived densities. In this section we discuss the uncertainties in the determination of electron densities using line ratios.

Figure 6 shows the derived densities for all the line ratios that vary significantly with density. We have omitted Fe XII λ200.36 since it is extremely far outside the limits. For this figure, lines which originate from the same upper level have been summed together. For this comparison we simply use the line emissivities at T_{max}, and, therefore, we exclude lines which are especially temperature-sensitive. All remaining values are plotted, as long as the full model and the simple emissivity ratio agree within 20% at the typical density of 10^{10} cm^{-3}. Ratios previously utilized as density diagnostics by Dere et al. (1979) are noted as solid circles in the figure. The figure indicates a number of line ratios that do not lie on the theoretical curves for intensity ratio versus N_e; most of these ratios are acceptable within a factor of 2 uncertainty. The remaining few that do not have already been discussed above as problematic.

While it is reassuring for most of the diagnostic line ratios to fall within the absolute bounds, given uncertainties, the large spread still appears disconcerting; however, we note that line ratios within factors of about 2 produce densities for Fe XV that are consistent with the average density, and that for Fe XII, the same is true except for line ratios involving λ335.06. We note that new predictions based on spectra observed from laboratory plasmas reject the identification of this line with Fe XII, placing the transition instead at λ335.33, where it is masked by the strong Fe XVI λ335.41 (Jupén, Isler, & Träbert 1993). For Fe XIII and Fe XIV the errors required to make the derived densities consistent would have to be somewhat larger, as one would expect from the ion by ion comparison in previous sections.

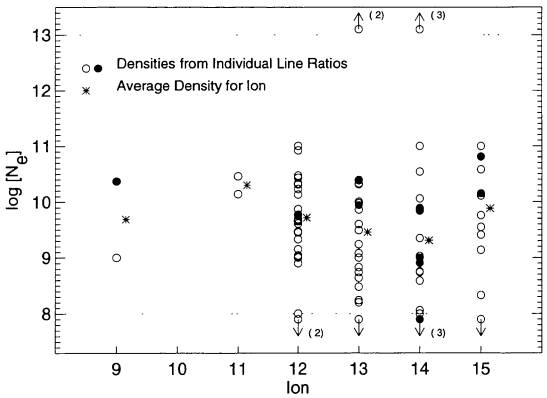

FIG. 6.—Electron densities derived for the SERTS active region spectrum, using different density-sensitive line ratios. The derived densities for each line ratio (both open and filled circles) are plotted vs. their relative ionization stages (e.g., 9 = Fe IX). The smaller set of solid circles are the diagnostics that have been used in previous observations, specifically in this case for the flares of Dere et al. (1979). The asterisks represent the average density for each ionization stage (offset for emphasis). The density range considered is from 10^8 to 10^{13} cm^{-3}. A number of the observed ratios lie somewhat above or below the theoretical curves for intensity ratio versus N_e: two points from Fe XII; three from Fe XIII; six from Fe XIV; and one from Fe XV. (The solid point below 10^8 for Fe XIV is among those that fall outside the range.) These "out-of-bound" ratios have not been included in the averages represented by the asterisks.

We note that the electron density derived for an active region from the Fe XII λ195.1/λ1242 line ratio (Withbroe & Raymond 1984) is now entirely consistent with the average density derived from the line ratios in the SERTS spectrum from Fe XII. As predicted by Withbroe & Raymond (1984) and demonstrated by Keenan, Tayal, & Henry (1990), the contribution of resonances to the effective collision strengths for the low-lying levels of Fe XII reduces this line ratio by approximately a factor of 3.

For the Capella data, the derived densities are not consistent with the expected uncertainties. The Fe XXI line ratios used have recently been discussed by Keenan et al. (1994a), who consider the solar flare data of Kastner, Neupert, & Swartz (1974), with the calibration curve of Mason et al. (1984). Their model ion is essentially the same as ours, incorporating the collision strengths of Aggarwal (1991). They derive electron densities consistent with each other within ±0.3 dex. Likely sources of error in the Capella data are statistical (for the weaker lines), blends, and identification. Furthermore, if the "bump" in the emission measure distribution reflects a high density component, the weighting of different density regions obviously compromises the technique.

We point out that our benchmark factor of 2 uncertainty for a line ratio includes estimates of the uncertainties in the atomic collision rates, as well as the observational errors. For some cases, this may overestimate the uncertainties in the atomic rates; however, it is important to keep in mind that all density-sensitive line intensity measurements are differently weighted averages over the range of emitting densities, for which the weighting factors are certainly nonlinear. Thus, we conclude that a large spread in derived densities is consistent with the combined uncertainties in the observations and the atomic models.

5. CONCLUSIONS

We have calculated new emissivities for Fe IX–XXIV, based on the ionization equilibrium balance of Arnaud & Raymond (1992) and newly compiled excitation rates. Comparisons with the SERTS catalog and the *EUVE* Capella spectrum, as well as various solar and tokamak spectra, show that our new model for highly ionized iron successfully predicts most of the observed line intensities, to within factors of ±35%.

This type of detailed spectral analysis can be a useful tool in the identification of spectral lines from observations. The model ions include all available radiative transition probabilities, and so the prediction of weak lines is a natural product of

the level population solution. The uncertainty analysis further strengthens the identification of a particular line. We identify four such previously unidentified lines from the SERTS spectrum (see Table 4): Fe XI λ406.84 and Fe XVII λ367.26, both of which are members of branching ratios listed in Table 3; Fe XIII λ313.0 in our model, observed at λ312.87; and Fe XV λ393.98.

A detailed comparison with other theoretical emissivity codes is made difficult by the differences in ionization balance and by different choices as to which weak lines to include and when to lump multiplets together. Spot checks suggest that our results are closer to the observations than are those of the Raymond & Smith code, Mewe et al. (1985) or Landini & Monsignori Fossi (1990). The relative intensities of lines of individual ions predicted by Landini & Monsignori Fossi scatter by a factor of 1.5–4 compared with our predictions for Fe X–XVI. For the lines of Fe XVIII–XXII, Landini & Monsignori Fossi predict higher emissivities by factors of 1.5–2. The new version of the Landini & Monsignori Fossi code, incorporating updated atomic rates, compares more favorably with the observations (Monsignori Fossi 1994).

We have shown the importance of the ionization equilibrium for comparing ions from different ionization stages. While our models provide only soft tests of the calculated balance, we have shown that rather large differences exist relative to models based on previously accepted rates. A comparison between EUV and X-ray lines (*EUVE* and *ASCA*) might provide more leverage to test the ionization balance. From a different perspective, we have not noted any discrepancies between observed and predicted line intensities that we attribute to problems with the assumption of ionization equilibrium.

The recent observations clear up a number of problems with previous observations. Unlike the solar flare observations discussed by Feldman (1992, 1993), the density diagnostic line ratio Fe IX λ241.74/λ244.91 in the SERTS spectrum is in good agreement with the densities derived from other ions. Fe XV λ284.15/λ417.24 is also within uncertainty limits, removing the need for departure from ionization equilibrium.

A major concern of this work has been to construct emission measure distribution models which adequately reflect the wealth of information contained in high-quality spectra. In particular, we have demonstrated that overreliance on a few strong line intensities may lead to errors on the order of factors of 2–3; the spread in the observed-to-predicted intensities for a given ion with several observed lines, indicates what confidence level one might expect. Furthermore, we have demonstrated the importance of integrating the emissivities over the entire temperature range, rather than assuming that the contribution to a line's intensity is necessarily confined to a narrow range of temperatures centered at the temperature of maximum ionization fraction.

It has not been important for our purposes here to evaluate the "best fit" of the emission measure distribution or to determine the confidence limits on the derived models; however, this task is clearly of interest for astrophysical applications. The most important input to such modeling will be the individual uncertainties for the observed line intensities. Smoothness constraints imposed in order to estimate the emission measure over temperature intervals with sparse data may lead to inadvertant smoothing over "real" features, such as the bump in Capella's emission measure distribution. It also appears necessary to evaluate the effect of step size in the temperature scale (we have used 0.1 dex).

With an understanding of the uncertainties in intensities, from both observational and theoretical sources, the uncertainties in electron densities derived from line ratios can be estimated. For a given ionization species, the derived densities may be consistent with each other to ±0.3–0.5 dex. Again we note that reliance on only a few line ratios from each ionization stage may lead to apparently large discrepancies.

The results of this analysis have important implications for further diagnostic work. Since we have calculated emissivities for a large number of weak lines, we can now predict weak lines which might be observed by EUVE for a source such as Capella. Specifically, the range of ions between Fe IX and Fe XV would help to validate the minimum in the emission measure distribution. While we have concentrated to date on iron, the determination of abundances would clearly benefit from the integrated emission measure method and a critical uncertainty analysis.

We thank the authors of the SERTS catalog for making their results available to us prior to publication. Roger Thomas has been generous in providing additional information about the instrument. We would also like to express our appreciation to the referee for a careful reading of the manuscript and many helpful suggestions. Discussions with Andrea Dupree have been invaluable. This work was supported by NASA grant NAGW-528 to the Smithsonian Astrophysical Observatory.

REFERENCES

Aggarwal, K. M. 1991, ApJS, 77, 677
Allen, C. W. 1973, Astrophysical Quantities (3d ed.; London: Athlone)
Arnaud, M., & Raymond, J. 1992, ApJ, 398, 394
Arnaud, M., & Rothenflug, R. 1985, A&AS, 60, 425
Behring, W. E., Cohen, L., Feldman, U., & Doschek, G. A. 1976, ApJ, 203, 521
Bhatia, A. K., & Doschek, G. A. 1992, Atomic Data Nucl. Data Tables, 52, 1
Bhatia, A. K., Feldman, U., & Seely, J. F. 1985, Atomic Data Nucl. Data Tables, 32, 461
———. 1986, Atomic Data Nucl. Data Tables, 35, 319
Bhatia, A. K., & Kastner, S. O. 1980, Sol. Phys., 65, 181
———. 1993, J. Quant. Spectrosc. Rad. Transf., 49, 609
Bhatia, A. K., & Mason, H. E. 1980, A&A, 83, 380
Boyd, W., Jelinsky, P., Finley, D. S., Dupuis, J., Abbott, M., Christian, C., & Malina, R. F. 1994, Proc. SPIE, 2280, in press
Bromage, G. E., Cowan, R. D., & Fawcett, B. C. 1977, Phys. Scripta, 15, 177
———. 1978, MNRAS, 183, 19
Burgess, A., Mason, H. E., & Tully, J. A. 1993, in UV and X-ray Spectroscopy of Laboratory and Astrophysical Plasmas, ed. E. Silver & S. Kahn (Cambridge: Cambridge Univ. Press), 97
Chen, M. H., & Reed, K. J. 1989, Phys. Rev. A, 40, 2292
Cheng, K. T., Kim, Y. K., & Desclaux, J. P. 1979, Atomic Data Nucl. Data Tables, 24, 111
Christensen, R. B., Norcross, D. W., & Pradhan, A. K. 1985, Phys. Rev. A, 32, 93
Corliss, C. & Sugar, J. 1982, J. Phys. Chem. Ref. Data, 11, 1

Dere, K. P. 1982, Sol. Phys., 75, 189
Dere, K. P., Mason, H. E., Widing, K. G., & Bhatia, A. K. 1979, ApJS, 40, 341
Doschek, G. A. 1984, ApJ, 279, 446
Doyle, J. G. 1987, Atomic Data Nucl. Data Tables, 37, 442
Dufton, P. L., & Kingston, A. E. 1991, Phys. Scripta, 43, 386
Dupree, A. K., Brickhouse, N. S., Doschek, G. A., Green, J. C., & Raymond, J. C. 1993, ApJ, 418, L41
Edlen, B., & Smitt, R. 1978, Sol. Phys., 57, 329
Faucher, P. 1977, A&A, 54, 589
Fawcett, B. C. 1984, Atomic Data Nucl. Data Tables, 31, 495
———. 1987, Atomic Data Nucl. Data Tables, 36, 141
———. 1991, Atomic Data Nucl. Data Tables, 47, 319
Fawcett, B. C., & Mason, H. E. 1989, Atomic Data Nucl. Data Tables, 43, 245
———. 1991, Atomic Data Nucl. Data Tables, 47, 17
Feldman, U. 1992, ApJ, 385, 758
———. 1993, Phys. Scripta, T46, 34
Feldman, U., Doschek, G. A., & Seely, J. F. 1985, MNRAS, 12, 41P
Feldman, U., Laming, J. M., Mandelbaum, P., Goldstein, W. H., & Osterheld, A. 1992, ApJ, 398, 692
Flower, D. R. 1977, A&A, 54, 163
Flower, D. R., & Nussbaumer, H. 1974, A&A, 31, 353
Flower, D. R., & Pineau des Fôrets, G. 1973, A&A, 24, 181
Foster, V. J., Keenan, F. P., & Reid, R. H. G. 1994, Phys. Rev. A, 49, 3092
Froese-Fischer, C., & Liu, B. 1986, Atomic Data Nucl. Data Tables, 34, 261
Fuhr, J. R., Martin, G. A., Wiese, W. L., & Younger, S. M. 1981, J. Phys. Chem. Ref. Data, 10, 305
Goldstein, W. H., Osterheld, A., Oreg, J., & Bar-Shalom, A. 1989, ApJ, 344, L37
Hayes, M. A. 1979, MNRAS, 189, 55P
Heil, T. G., Kirby, K. & Dalgarno, A. 1983, Phys. Rev. A, 27, 2826
Huang, K.-N. 1986, Atomic Data Nucl. Data Tables, 34, 1
Idrees, M., & Das, B. P. 1989, J. Phys. B, 22, 3609
Jupén, C., Isler, R. C., & Träbert, E. 1993, MNRAS, 264, 627
Kastner, S. O., Neupert, W. M., & Swartz, M. 1974, ApJ, 191, 261
Keenan, F. P., Conlon, E. S., Warren, G. A., & Aggarwal, K. M. 1994a, Sol. Phys., 149, 129
Keenan, F. P., Conlon, E. S., Warren, G. A., Boone, A. W., & Norrington, P. H. 1993, ApJ, 406, 350
Keenan, F. P., Foster, V. J., Brown, P. J. F., Thomas, R. J., Neupert, W. M., Davila, J. M., & Tayal, S. S. 1995, in preparation
Keenan, F. P., Tayal, S. S., & Henry, R. J. W. 1990, Sol. Phys., 125, 61
Keenan, F. P., Thomas, R. J., Neupert, W. M., & Conlon, E. S. 1994b, Sol. Phys., 149, 301
Kim, Y. K., & Cheng, K. T. 1978, J. Opt. Soc. Am., 68, 836
Landini, M., & Monsignori Fossi, B. C. 1990, A&AS, 82, 229
Lang, J., ed. 1994, Atomic Data Nucl. Data Tables, 57, nos. 1/2
Lang, J., Mason, H. E., & McWhirter, R. W. P. 1990, Sol. Phys., 129, 31
Linsky, J. L., et al. 1993, ApJ, 402, 694
Loulergue, M., Mason, H. E., Nussbaumer, H., & Storey, P. J. 1985, A&A, 150, 246
Loulergue, M., & Nussbaumer, H. 1975, A&A, 45, 125
Malinovsky, M., & Heroux, L. 1973, ApJ, 181, 1009
Mann, J. B. 1982, private communication
———. 1983, Atomic Data Nucl. Data Tables, 29, 407
Mason, H. E. 1975, MNRAS, 170, 651
Mason, H. E., Bhatia, A. K., Kastner, S. O., Neupert, W. M., & Swartz, M. 1984, Sol. Phys., 92, 199
Mason, H. E., Doschek, G. A., Feldman, U., & Bhatia, A. K. 1979, A&A, 73, 74
Mason, H. E., & Nussbaumer, H. 1977, A&A, 54, 547
Mason, H. E., & Storey, P. J. 1980, MNRAS, 191, 631
Mewe, R. 1991, Astron. Astrophys. Rev., 3, 127
Mewe, R., Gronenschild, E. H. B. M., & van den Oord, G. H. J. 1985, A&AS, 62, 197
Mohan, M., Baluja, K. L., Hibbert, A., & Berrington, K. A. 1987a, MNRAS, 225, 377
———. 1987b, J. Phys. B, 20, 6319
Monsignori Fossi, B. 1994, private communication
Neupert, W. M., Epstein, G. L., & Thomas, R. J. 1992, Sol. Phys., 137, 87
Pradhan, A. K. 1988, Atomic Data Nucl. Data Tables, 40, 355
Pradhan, A. K., & Gallagher, J. W. 1992, Atomic Data Nucl. Data Tables, 52, 227
Raymond, J. C. 1988, in Hot Thin Plasmas in Astrophysics, ed. R. Pallavicini (Dordrecht: Kluwer), 3
Raymond, J. C., & Smith, B. W. 1977, ApJ, 35, 419
Redfors, A. & Litzen, U. 1989, J. Opt. Soc. Am., B6, 1447
Reed, K. J., Chen, M. H., & Hazi, A. U. 1987, Phys. Rev. A, 36, 3117
Rugge, H. R., & McKenzie, D. L. 1985, ApJ, 297, 338
Seaton, M. J. 1987, J. Phys. B., 20, 6363
Smith, B. W., Raymond, J. C., Mann, J. B., & Cowan, R. D. 1985, ApJ, 298, 898
Stratton, B. C., Moos, H. W., & Finkenthal, M. 1984, ApJ, 279, 31
Stratton, B. C., Moos, H. W., Suckewer, S., Feldman, U., Seely, J. F., & Bhatia, A. K. 1985, Phys. Rev. A, 31, 2534
Summers, H. P. 1974, Culham Laboratory, Internal Memo, 367
Svensson, L. A., Ekber, J., & Edlen, B. 1974, Sol. Phys., 34, 173
Tayal, S. S. 1994, ApJ, 426, 449
Tayal, S. S., & Henry, R. J. W. 1986, ApJ, 302, 200
———. 1988, ApJ, 329, 1023
Tayal, S. S., Henry, R. J. W., & Pradhan, A. K. 1987, ApJ, 319, 951
Thomas, R. J. 1994, private communication.
Thomas, R. J., & Neupert, W. M. 1994, ApJS, 91, 461.
Vernazza, J. E., & Raymond, J. C. 1979, ApJ, 228, L89
Waljeski, K., Moses, D., Dere, K. P., Saba, J. L. R., Strong, K. T., Webb, D. F., & Zarro, D. M. 1994, ApJ, 429, 909
Welsh, B. Y., Vallerga, J. V., Jelinsky, P., Vedder, P. W., Bowyer, S., & Malina, R. F. 1990, Opt. Eng., 29, 752
Withbroe, G. L., & Raymond, J. C. 1984, ApJ, 285, 347
Zhang, H. L., & Sampson, D. H. 1994, Atomic Data Nucl. Data Tables, 56, 41.